NTNU – Trondheim
Norwegian University of
Science and Technology

Numerical Simulation of Flow around Single and Two side-by-side Square Cylinders with Horizontal Offsets Mounted on the Seafloor

Yukun DAI

June 2016

Supervisor 1: Professor Dag Myrhaug

Supervisor 2: Research Professor Lars Erik Holmedal

Supervisor 3: Dr. Hong Wang

Department of Marine Technology

Norwegian University of Science and Technology

Preface

This master thesis is the summary of my study during the two-year master education in Marine Technology at the Norwegian University of Science and Technology (NTNU).

At first, I would like to thank Pro. Dag Myrhaug, Dr. Lars Erik Holmedal and Dr. Hong Wang for their encouragements and patient guidance. Without their instructions, this thesis would never be finished.

A special thanks to HPC Group for their excellent high performance PC Vilje to help me save a lot of time.

Last but not least, Thanks to my friends and family, who support me to overcome the difficulties and barriers in these two years

Trondheim, 2016-06-20

Yukun DAI

NTNU Trondheim
Norwegian University of Science and Technology
Department of Marine Technology – Group of Marine Structures

MASTER THESIS IN MARINE TECHNOLOGY

SPRING 2016

FOR

STUD. TECHN. YUKUN DAI

NUMERICAL SIMULATION OF FLOW AROUND SINGLE AND TWO SIDE-BY-SIDE SQUARE CYLINDERS WITH HORIZONTAL OFFSETS MOUNTED ON THE SEAFLOOR

Square cylinders may represent idealized roughness elements on the seafloor. These structural components are most often subject to turbulent flow. Computational Fluid Dynamics (CFD) represents an efficient tool to obtain the essential hydrodynamic quantities of interest.

The student shall:

1. Give a background of CFD and flow around bluff bodies
2. Describe the computational tools
3. Give a background description of turbulence modelling
4. Perform numerical simulations of the flow around single and two side-by-side square cylinders with horizontal offsets mounted on the seafloor
5. Present and discuss the results

The work scope may prove to be larger than initially anticipated. Subject to approval from the supervisor, topics may be deleted from the list above or reduced in extent.

In the thesis the candidate shall present his personal contribution to the resolution of problem within the scope of the thesis work.

Theories and conclusions should be based on mathematical derivations and/or logic reasoning identifying the various steps in the deduction.

The candidate should utilize the existing possibilities for obtaining relevant literature.

The thesis should be organized in a rational manner to give a clear exposition of results, assessments, and conclusions. The text should be brief and to the point, with a clear language. Telegraphic language should be avoided.

The thesis shall contain the following elements: A text defining the scope, preface, list of contents, summary, main body of thesis, conclusions with recommendations for further work, list of symbols and acronyms, reference and (optional) appendices. All figures, tables and equations shall be numerated.

The supervisor may require that the candidate, in an early stage of the work, present a written plan for the completion of the work. The plan should include a budget for the use of computer and laboratory resources that will be charged to the department. Overruns shall be reported to the supervisor.

The original contribution of the candidate and material taken from other sources shall be clearly defined. Work from other sources shall be properly referenced using an acknowledged referencing system.

Advisors: Dr. Hong Wang
Research Professor Lars Erik Holmedal
Professor Dag Myrhaug

Deadline: 10.06.2016

Dag Myrhaug

Dag Myrhaug
Supervisor

Abstract

Computational Fluid Dynamics (CFD) have been applied to obtain essential hydrodynamic quantities and flow behaviors of single and two 2D wall-mounted square cylinders subjected to a uniform turbulent inflow. This is a simplified model for flow around sea bed roughness. Sea bed roughness alters the flow near the sea floor and creates unique wakes. An analysis to the flow phenomenon in this process is relevant for the safety and stability of pipelines, platform and etc.

Reynolds number based on the dimension of the square cylinder is 4000 in this study. Numerical simulations of uniform flow around single wall-mounted square cylinder and two wall-mounted square cylinder with three intervals of $L = h$, $L = 2h$ and $L = 5h$ have been performed. The solutions of pressure distribution, velocity distribution and streamlines were discussed. Since no periodic flow phenomenon was observed during the simulations, the present study is considered to be steady-state.

The square cylinders are directly placed on the sea bed. The geometries (upstream length, downstream length and height) of the domain was defined to eliminate any far-field effects and to ensure the domain-size independence.

Two dimensional Reynold Averaged Navier Stokes (RANS) equations with standard $k-\omega$ turbulence model were applied. The open source CFD software OpenFOAM was used to meshand solve the flow field. Post-processing software Tecplot was utilized to visualize the results.

The convergence tests for flow around one cylinder and flow around two cylinders with three intervals have been performed. The solutions of mean drag coefficient C_D and mean lift coefficient C_L in steady-state were used to test the mesh convergence. The mesh convergence for both two cases have been demonstrated.

Results from the simulation for flow around single square cylinder have been discussed. The

simulation predicted the flow phenomena that correspond to the experiment, which validates the numerical set-up in this study.

A study of the effect of the interval between two wall-mounted square cylinders was conducted. After the comparison of force coefficients, pressure and velocity field, the strongest interaction between the two cylinders was in the case 1 with $L = h$, where unique reattachment and cavity flow were found inside the interval. However, with the increasing interval, the reattachment and the cavity flow disappear and the two cylinders become independent in the cases with $L = 2h$ and $L = 5h$. The weakest interaction was found for the case 3 with $L = 5h$, in which the resulting drag coefficient C_D showed less than 5% and the lift coefficient showed less than 8% difference relative to the one cylinder simulation. The formations of each vortex, low pressure and low velocity zone have been explained.

The present RANS simulations predict flow behaviors reasonably. The possible influences of sea bed roughness on the fluid are also successfully predicted.

List of symbols

A	$[m^2]$	Projected area of the body
A_s	[-]	Area coefficient
A^*	[-]	Dimensionless coefficients in the expression of J^*
B	[-]	Constant coefficient in wall function
B^*	[-]	Dimensionless coefficients in the expression of J^*
C_D	[-]	Drag coefficient
C_L	[-]	Lift coefficient
D	$[m]$	Diameter of cylinder
D_k	[-]	Diffusion term in the k-equation
f	[-]	Component of the convective or diffusive vector that normal to CV faces
F	$[kg/m^2]$	Total mass flow rates through CV faces
F_D	$[N]$	Drag force
F_L	$[N]$	Lift force
f_v	$[s^{-1}]$	Vortex shedding frequency
G	$[m]$	Gap of cylinder to sea bed
h	$[m]$	Height of the square cylinder
H_D	$[m]$	Height of the domain
J_x, J_y	$[kg/(m \cdot s^2)]$	Total momentum fluxes in x and y direction of a CV
J^*	$[m/s]$	Modified momentum fluxes
k	$[m^2/s^2]$	Mean turbulent kinetic energy
l	$[m]$	Length scale
L	$[m]$	Offset (Interval) of the cylinders
L_b	$[m]$	Characteristic length of the body
L_d	$[m]$	Downstream length of the domain
L_u	$[m]$	Upstream length of the domain
P	$[N/m^2]$	Mean pressure
P_e	[-]	Peclet number
P_k	[-]	Production term in the k-equation
p^*	$[N/m^2]$	Guessed pressure field
p'	$[N/m^2]$	Pressure correction
$\tilde{P}$	$[N/m^2]$	Hydrodynamic pressure
q_ϕ	[-]	Inner density change of ϕ
Re	[-]	Reynold number

S	[-]	Source terms in the discretization equations
s_{ij}	$[N/m^2]$	Turbulent stress tensor
S_{ij}	$[s^{-1}]$	Mean strain tensor
St	[-]	Strouhal number
$\tilde{S}_{ij}$	$[s^{-1}]$	Instantaneous rate of strain
t	$[s]$	Instantaneous time
T	$[s]$	Characteristic length of time that larger than any flow phenomenon
u	$[m/s]$	Fluctuating velocity
U	$[m/s]$	Mean velocity
U_i, U_j	$[m/s]$	Velocity components in i and j direction
U_s	$[m/s]$	Velocity on the body surface
U_∞	$[m/s]$	free stream velocity far away from the cylinder
u^*	$[m/s]$	Guessed velocity field in x direction
$u^{'}$	$[m/s]$	Velocity correction in x direction
u^+	$[m/s]$	Non-dimensional mean velocity
$\hat{U}$	$[m/s]$	Characteristic free stream velocity
$\tilde{U}$	$[m/s]$	Instantaneous velocity
V	$[m/s]$	Velocity scale
v^*	$[m/s]$	Guessed velocity field in y direction
$v^{'}$	$[m/s]$	Velocity correction in y direction
x_i, x_j	$[m]$	Cartesian Coordinates in i and j direction
y^+	$[m]$	Non-dimensional distance to the wall
α	[-]	Phase angle
$\alpha 1$	[-]	Proportion coefficient in the equation of J^*
β_k	[-]	Closure coefficient for the k-equation
γ_k	$[m^2/s]$	Turbulent or eddy diffusivity
δ_{ij}	[-]	Kronecker delta
ϵ	$[m^2/s^3]$	Dissipation rate of energy in the k-equation
η	$[m]$	Kolmogorov microscales
κ	[-]	Von Karman constant
μ	$[kg/(m\cdot s)]$	Dynamic viscosity
μ_t	$[kg/(m\cdot s)]$	Turbulent dynamic viscosity
ν	$[m^2/s]$	Kinematic viscosity
ν_T	$[m^2/s]$	Turbulent/eddy-viscosity
ρ	$[kg/m^3]$	Density of flow
$\tilde{\sigma}_{ij}$	$[N/m^2]$	Instantaneous stress tensor
Σ_{ij}	$[N/m^2]$	Mean stress tensor
σ_k	[-]	Closure coefficients for the k-equation
σ_ω	[-]	closure coefficient for the transport equation of ω
τ_{ij}	$[N/m^2]$	Reynold stress
τ_w	$[N/m^2]$	Wall shear stress
ϕ	[-]	Flow quantity
Ω	$[m^3]$	Volume of CV
ω	$[s^{-1}]$	Specific dissipation rate

Acronyms

2D Two Dimensional

3D Three Dimensional

CDS Linear Interpolation

CFD Computation Fluid Dynamics

CV Control Volume

DNS Direct Numerical Simulation

GPL General Public License

LES Large Eddy Simulation

LUDS Linear Upwind Scheme

PIV Particle Image Velocimetry

QUICK Quadratic Upwind Interpolation

RANS Reynold Averaged Navier Stokes

SUS Skew Upwind Scheme

UDS Upwind Interpolation

Contents

Chapter 1

Introduction

1.1 Background and motivation

With increasing demand of energy and resources, oil and gas in land can not satisfy the need of industrial development. People start to explore the resources in the deep ocean.Therefore, Countless complex offshore structures have been constructed in past several decades, such as oil drilling platforms and wind turbines. Most of them are jacket and single-leg platforms in the coastal area. Pipelines connect them together and transport oil and gas to the inland. These structures normally have direct links to sea bed. Thus, when it comes to the safety of offshore structures, sea bed plays an important role. A great number of models for offshore structures under waves and current have been proposed, but most of them simplify the sea bed as smooth wall and consider perfect turbulent boundary layer. This assumption does not account sea bed roughness: complex terrain of sea bed alters the inflow and indirectly changes the hydrodynamic forces on the structures. A comprehensive understanding of sea bed roughness is vital for the safety and construction of the offshore structures.

A common simplified model for the sea bed roughness is cube. Cube is one of the simplest geometries with bluff corners, which is similar to the sea bed roughness. Compared with flow aroundg cylinder, flow around cube separates at fixed points (bluff corners) instead of flow-dependent positions; steady but not periodic vortices and recirculations are generated after flow separation.

Besides, the sea bed roughness is tiny structure. Therefore, Boundary layer on the sea bed is

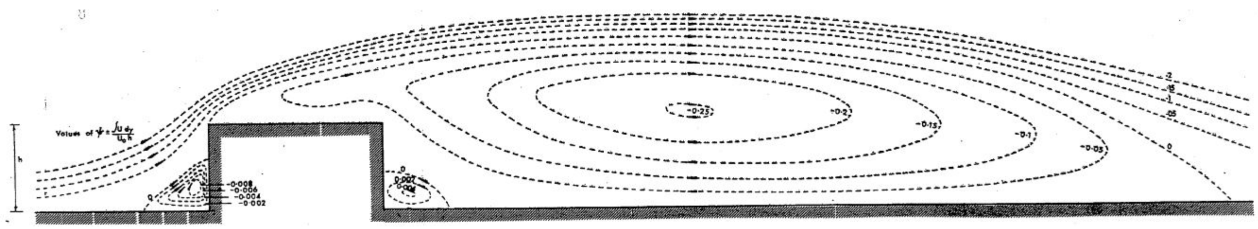

Figure 1.1: Streamlines from wind tunnel test by Moss and Baker (1980)

comparable to the roughness in height. Consequently, Reynolds number based on the dimension of the roughness is small. A low-Re model should be adopted, which is the main difference compared with other high-Re flow simulations.

1.2 Literature review

Flow around wall-mounted Three Dimensional (3D) cube or Two Dimensional (2D) square cylinder have been investigated for a long time. Owe to its simplicity and predictability, it has becoming the benchmark test for the validation of new model and new method. Castro and Robins (1977) measured the mean surface pressure, mean and fluctuating velocities around a surface-mounted cube in a uniform upstream flow and a simulated atmospheric boundary layer; Hoxey et al. (2002) conducted experiments on cubes with different angles of windward face in atmospheric boundary layer; Sousa (2002) used a new Particle Image Velocimetry (PIV) method to measure the velocity field around a surface-mounted cube. All above experiments have observed the deflection of inflow, flow separated and several recirculation areas.

Figure 1.1 presented the wind tunnel test of flow around 2D square cylinder by Moss and Baker (1980)). It can be seen that a large recirculation zone formed behind the cylinder. After the recirculation zone, the separated flow reattachs the wall far away behind the cylinder. it is also observed that two small recirculation zones are formed at two downward corners of the cylinder.

With the increasing computational performance, Computational Fluid Dynamics (CFD) becomes an wide-accepted alternative method to experiment in fluid dynamics. CFD has some obvious advantages over the experiment: the field configurations and flow parameters can be easily adjusted in the computer; CFD is high efficient and requires a lower cost; some environmental conditions which are difficult to introduce in lab can be achieved in computer. These advantages make CFD a common tool in hydrodynamics analysis recent years. Most of the CFD are based on the combination of Reynolds Averaged Navier Stokes equations (RANS) and turbulence models. RANS applies eddy viscosity theory and relates the turbulence with the mean flow by turbulent viscosity, while turbulence model helps to resolve the eddy viscosity (Iaccarino et al. (2003);Lakehal and Rodi (1997); Baetke et al. (1990)).

However, At a high Reynolds number (defined in Equation 2.1), the flow around a bluff body is complex due to the generation of turbulent eddies and the detachment of boundary layer. The normal RANS method is hard to deal with such problems (Roy et al. (2003)). Instead, benefiting from the rapid development of computational capability, Large-Eddy Simulation (LES) and Direct Numerical Simulation (DNS) are preferable in recent years.

In the turbulent flow, one of the most important concepts is Kolmogorov microscale η, which is defined as the smallest eddy scale in the flow. Its expression is (Landahl and Mollo-Christensen (1992))

$$\eta = \left(\frac{\nu^3}{\varepsilon}\right)^{\frac{1}{4}} \tag{1.1}$$

where ν is the kinematic viscosity and ε is the rate of kinetic energy dissipation. Because the turbulent flow models (RANS, LES and DNS)are based on the resolution of Navier Stokes equations (Equation2.11). If we do not use the turbulence model and the eddy-viscosity concept, the full resolution of the Navier Stokes equations requires a dimension of mesh grid that smaller than the Kolmogorov microscale. This is how DNS works, e.g. Yakhot et al. (2006) has calculated flow around a wall mounted 3D cube with DNS method.

However, the Kolmogorov microscale is too small. it is estimated that a three-dimensional DNS requires a number of mesh grids proportional to $Re^{2.25}$. This is unaffordable in most cases.

To reduce computational consumption, LES is proposed. LES was first proposed by Smagorinsky (1963), with the introduction of Smagorinsky subgrid scale. The kernel of the LES is to reduce the range of turbulence scales that are numerically resolved by adapting a low-pass filtering function. Low-pass filtering indicates that the filtering function would remove small-scale information from the numerical solution. These filtered small-scale eddies are modelled, and the other larger-scale eddies are numerically resolved by the Navier Stokes equations. Thus, it

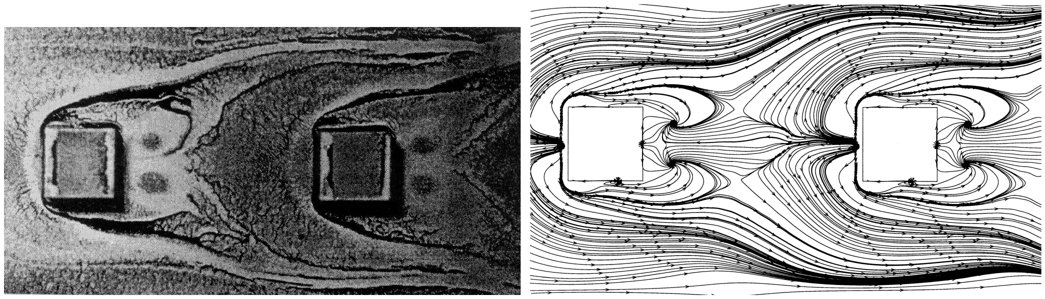

Figure 1.2: Surface streamlines of the time-averaged flow for double cubes; Left: oil picture from experiment; Right: LES simulation. (Stoesser et al. (2003))

becomes possible to apply LES under the present status of computational capability. For instance, Lim et al. (2009) has presented a numerical simulation about flow around a mounted surface cube placed in a turbulent boundary layer by LES, and matched the results with wind tunnel observations; Murakami and Mochida (1995) applied LES to calculate flow around a 3D cube and a 2D square cylinder;

1.3 Problem Formulation

Most of the investigations about cube/square cylinder focus on the flow behavior around single body. However, it is common in nature that sea bed roughness is diverse and continuous. Different values of roughness can be simplified to multiple cubes/square cylinders with various intervals. For example, a smooth sea bed is simplified to cubes/square cylinders with infinite interval; a high rough sea bed is modelled by cubes/square cylinders with small interval. If we look at the flow around two cubes in Figure 1.2, the wakes generated by the first cube alter the flow and create distinct inflow to the subsequent cube. The resultant forces and flow fields around the first and second cube are entirely different. In this type of flow, the interval plays an important role. Compared with Figure 1.1, we can see the wake flow is sensitive to the length of interval. Thus, an investigation to interaction between these cubes/square cylinders is necessary.

Based on the ideas illustrated above, this study focuses on a uniform flow around two side-by-side 2D square cylinders with different horizontal offsets mounted on the sea bed and conducts a series of numerical simulations. Normally, it is ideal to use LES or DNS method, but

RANS model can also produce result with enough accuracy. In considerations of limited computational capability and the short period of master thesis, the least expensive RANS model with $k-\omega$ turbulence model is applied in this study.

The case of flow around one sqaure cylinder is studied first. Then flow around two square cylinders are investigated. The results of different offsets (intervals) are discussed compared with each other. The simulations were finished by open source software OpenFOAM

1.4 Structure of the thesis

The thesis is structured as follows.

Chapter 1 gives an background introduction to the topic and motivation.

Chapter 2 presents a review of flow properities, turbulent boundary layer and the theory of turbulence.

Chapter 3 describes the concept of CFD, the computational tools and the algorithms inside OpenFOAM.

Chapter 4 explains the domain, mesh set-up and boundary conditions.

Chapter 5 presents the results and discussions of numerical simulation of flow around one sqaure cylinder and flow around two sqaure sylinders with three different intervals.

Chapter 6 gives the conclusion and recommendation of future work to the master thesis.

Chapter 2

Theory

This chapter presents an introduction to the basic theory of flow passing a body in laminar and turbulent flow, including assumptions and governing equations to solve the flow. The simulation method and the turbulence model applied in this study are clarified.

2.1 Flow separation

The main factors influencing the flow (air or water) can be characterized by the Reynolds number, which is the ratio of inertia force to viscous force

$$\mathrm{Re} = \frac{\text{inertia force}}{\text{viscous force}} = \frac{\hat{U} L_b}{\nu} \tag{2.1}$$

where $\hat{U}$ is the characteristic free stream velocity, L_b is the characteristic length of the body, and ν is the kinetic viscosity. Other factors such as body form, the sea floor effects and the free surface effect are also important, but Reynolds number determines general behaviors of flow.

At first, we consider flow around a circular cylinder in infinite water depth, low-Re laminar flow and without the free-surface effect, which is defined in Figure 2.1. If we consider potential flow theory and integrate the pressure along the surface of cylinder, the integrated forces in all directions are zero. This is a contrast to the experiment where drag force exists in the flow direction and periodic lift force exists in the crosswise direction, something should happen when flow passes the cylinder.

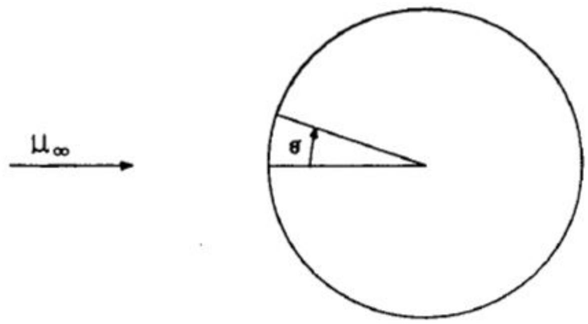

Figure 2.1: Definition of steady flow past a circular cylinder, U_∞ is the free stream velocity far away from the cylinder (Faltinsen (1993)).

It is known that there is a boundary layer along the cylinder surface. Inside the boundary layer, flow velocities decrease from the free stream velocity at the top layer to zero at the surface of body to maintain non-slip boundary condition. The velocity distribution across the boundary layer can be calculated from boundary layer equations (Schlichting (1968)) and is shown in Figure 2.2.

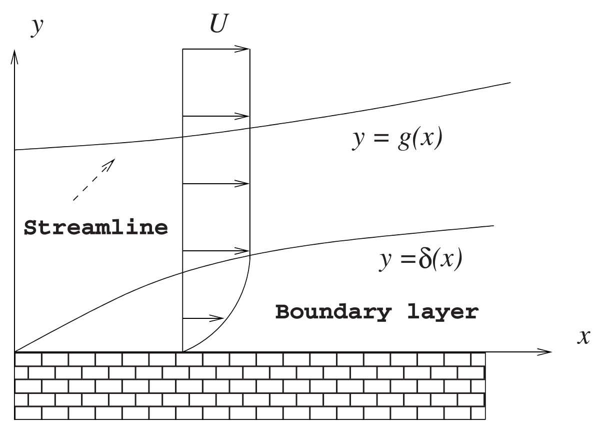

Figure 2.2: Velocity distribution inside the boundary layer (Pozrikidis (2009))

Flow separation means the flow breaks strongly away from the body. At a point on the cylinder surface there is back-flow on the upstream side of that point, and the velocity on the body surface U_s satisfies

$$\frac{\partial U_s}{\partial y} = 0 \tag{2.2}$$

at that point. After the flow separation point, the pressure on the surface drops rapidly. Consequently, the integrals of pressure along the surface before and after the separation point are quite different, which create the drag force in the flow direction. For the convenience to express drag force on a body induced by flow, we define an non-dimensional coefficient to represent the drag force, which is called drag coefficient C_D

$$C_D = \frac{F_D}{\frac{1}{2}\rho \hat{U}^2 A} \tag{2.3}$$

where F_D is the drag force on the body, ρ is the density of flow, and A is the projected area of the body.

2.2 Vortex shedding

After the separation, the flow is unsteady and eddies are shed from each side of the cylinder and convected with the flow. In the starting process of separated flow around a circular cylinder, symmetric wakes develops, but it only happens at a very low Reynolds number. With increasing Reynolds number, the extreme instability of separated flow causes asymmetric wakes. The consequence is that vortices are alternatively shed from each side of the cylinder, Figure 2.2 illustrates this process. The non-dimensional vortex shedding frequency may be represented by

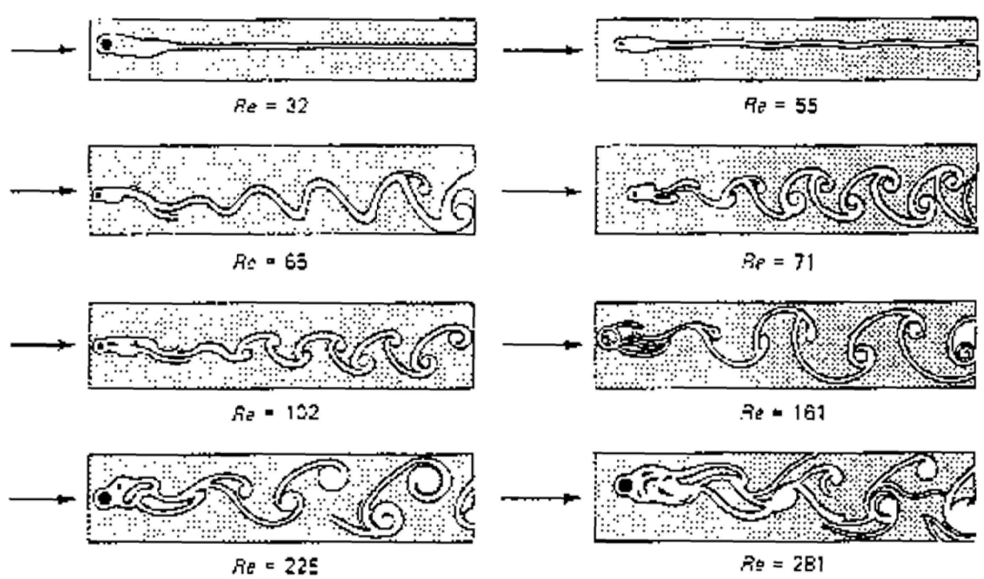

Figure 2.3: The development of vortex shedding (Homann (1936))

Strouhal number(St), which is defined by

$$St = \frac{f_v D}{\hat{U}} \tag{2.4}$$

where D is the diameter of cylinder, f_v is the vortex shedding frequency.

Because of the periodic shedding of vortices, the body endures oscillatory forces both in the streamwise and crosswise direction. The streamwise force corresponds to drag force and the crosswise force corresponds to lift force. If there is only a single vortex shedding frequency, the lift force F_L can be approximated by

$$F_L(t) = |F_L| \cos\left(2\pi f_v + \alpha\right) \tag{2.5}$$

where α is phase angle. The lift force amplitude $|F_L|$ is normally expressed by lift coefficient C_L, which is defined by

$$C_L = \frac{|F_L|}{\frac{1}{2}\rho \hat{U}^2 A} \tag{2.6}$$

2.3 Wall effects

Until now, the flow behaviors we discussed are limited to the condition of infinite water depth. The interaction of the shear layers shed from the top and the bottom half of the cylinder is the characteristic of vortex shedding happening in this condition. If a sea bed is considered, its boundary layer can reduce or inhibit this interaction, even alter and prevent the vortex shedding.

Figure 2.4 shows the streamlines of a cylinder in infinite water depth and close to sea bed. In the presence of sea bed, the stagnation point, defined as the point on the cylinder that has zero velocity at the top of boundary layer, becomes closer to the sea bed. The separation point on the upper half of the cylinder moves downstream while the one on the lower half of the cylinder moves downstream. This results in the asymmetry of vortices shed from the two sides of the cylinder. The upper vortex grows larger and stronger than the other one. Vortex shedding disappears due to the strength difference between these two vortices.

The gap to the sea bed (G) is also an important parameter that determines the flow behavior.

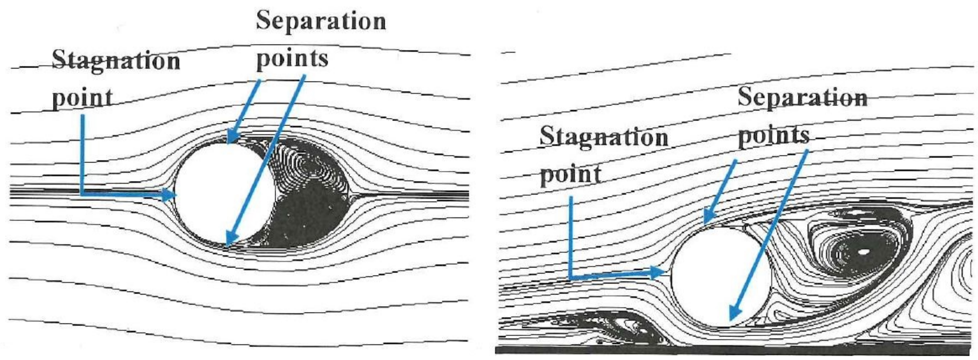

Figure 2.4: Time-averaged streamlines for the flow around a cylinder. *Re*=13100. Left: in the infinite water; Right: with sea bed (Prsic (2016)).

Bearman and Zdravkovich (1978) recognized that the vortex shedding ceases to exist for a gap to cylinder diameter ration G/D of about 0.3, which is a clear limit for the vortex shedding suppression. In Figure 2.5, Bearman and Zdravkovich (1978) presented photographs of the flow pattern for G/D=0.2 and 1.0, they are the representative cases for narrow and wide gap flow. The vortex shedding is absent for the narrow gap case and there is extremely asymmetric and upwards deflected wake. While the wide gap allows the fluid to flow more freely, the downstream eddies are strong and equally spaced, and the vortex shedding frequency does not have significant changes.

Eventually, if the cylinder is directly placed on the sea bed, the vortex shedding should disappear and there would be only one strong vortex generated from the upper half of the cylinder. In the present study, flow around a 2D square cylinder instead of circular cylinder is studied. It can be expected that there is only one strong vortex generated from the square cylinder and periodic vortex shedding doesn't happen. Thus we can assume the simulation to be steady-state, which means the present study is time-independent.

2.4 Turbulence

Turbulent flow need to be applied when the Reynolds number exceeds a specified range usually in the order of 10^3. Most flows occurring in nature are turbulent, as well as in many relevant engineering applications. Current in the deep ocean is turbulent; Boundary layer growing on the surface of a riser is turbulent; Rivers also usually have turbulent flow. Turbulent flow is

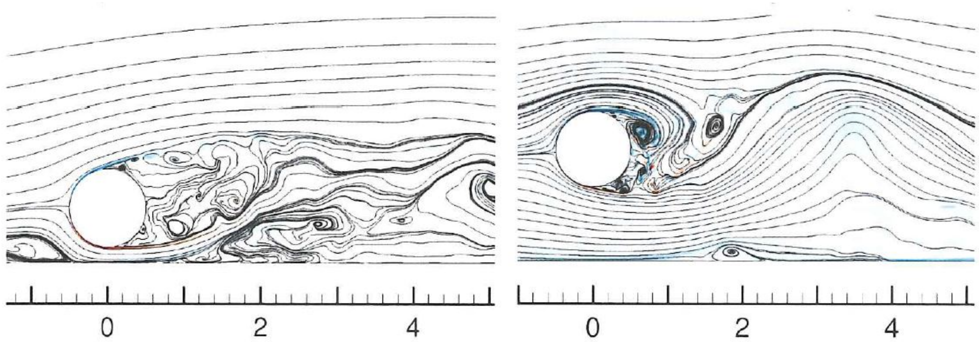

Figure 2.5: Instantaneous flow patterns for Re=13100. Left: G/D=0.2; Right: G/D=1.0 (Prsic (2016)).

extremely complex and even hard to define precisely. But we can give some characteristics of the turbulent flow (Tennekes and Lumley (1972))

1. The randomness feature of turbulent flow makes statistical methods the only way to model turbulence, which is the result of irregularity of turbulence.

2. The diffusivity of turbulence mixes the momentum and heat of fluids. This kind of mixing and transfer of mass and heat makes properties that are related to fluid transport, which is important and need to be included in the model of turbulence.

3. Turbulent flow always exhibits at a high Reynolds number, which means a high level of fluctuation. The generation of eddies needs to be modelled.

In contrast to instantaneous value of flow properties, mean quantities are more significant for turbulent flow investigation. (the following derivation is abstracted from Tennekes and Lumley (1972)) The governing equations for incompressible fluid are

$$\frac{\partial \tilde{U}_i}{\partial t} + \tilde{U}_j \frac{\partial \tilde{U}_i}{\partial x_j} = \frac{1}{\rho} \frac{\partial}{\partial x_j} \tilde{\sigma}_{ij} \tag{2.7}$$

$$\frac{\partial \tilde{U}_i}{\partial x_i} = 0 \tag{2.8}$$

where the subscripts i and j follow the Einstein notation that when an index variable appears twice in a single term and is not otherwise defined, the notation implies summation of that term over all the values of the index. In the Cartesian coordinate system, the indices i and

j range over the set $\{1, 2, 3\}$ corresponding to x, y and z-direction; $\tilde{\sigma}_{ij}$ is the stress tensor. The tilde on top of the terms represent instantaneous value of the flow properties, e.g. $\tilde{U}$ represents instantaneous value of flow velocity. It should be noted that we also define $\hat{U}$ which is the free stream velocity, and that they are different quantities.

If the fluid is Newtonian, the stress tensor $\tilde{\sigma}_{ij}$ is expressed by

$$\tilde{\sigma}_{ij} = -\tilde{P}\delta_{ij} + 2\mu\tilde{S}_{ij} \tag{2.9}$$

where δ_{ij} is the Kronecker delta. It equals to one when $i = j$ and equals to zero in all other cases; $\tilde{P}$ is the hydrodynamic pressure and μ is the constant dynamic viscosity. The expression for the rate of strain $\tilde{S}_{ij}$ is

$$\tilde{S}_{ij} = \frac{1}{2}\left(\frac{\partial \tilde{U}_i}{\partial x_j} + \frac{\partial \tilde{U}_j}{\partial x_i}\right) \tag{2.10}$$

Substitute Equation 2.9 to Equation 2.7, we obtained

$$\frac{\partial \tilde{U}_i}{\partial t} + \tilde{U}_j \frac{\partial \tilde{U}_i}{\partial x_j} = -\frac{1}{\rho}\frac{\partial \tilde{P}}{\partial x_i} + \nu \frac{\partial^2 \tilde{U}_j}{\partial x_j \partial x_j} \tag{2.11}$$

where ν is the kinematic viscosity.

The resulting Equation 2.11 is the so-called Navier-Stokes equation, it is the starting point to solve any flow problems, including turbulent flow. However, Equation 2.11 is specified for instantaneous quantities, but it is the mean quantities of flow that are meaningful in engineering problems. Therefore, in order to obtain the governing equations for mean velocity, the so-called Reynolds decomposition is applied.

2.5 Reynolds Averaged Navier Stokes (RANS) equation

The instantaneous flow velocity $\tilde{U}$ can be decomposed into the summation of a mean flow and a fluctuating velocity by Reynolds decomposition

$$\tilde{U} = U + u \tag{2.12}$$

where U is the mean component of velocity, and u is the fluctuating component of velocity. This decomposition isolates the effect of turbulence, which makes it easier to calculate the mean flow.

The mean flow velocity U should be independent of time and fulfills

$$\frac{\partial U_i}{\partial t} = 0 \tag{2.13}$$

while the mean fluctuating velocity should be equal to zero if we average the fluctuating velocity u over an enough long time T which should larger than any flow phenomena

$$\bar{u} = \frac{1}{T}\int_0^T u(t)dt = 0 \tag{2.14}$$

Similarly, the pressure, strain tensor and stress tensor can be divided into a mean component plus a fluctuating component by Reynolds decomposition, while the time averaging values of the fluctuating component also equal to zero.

According to the Reynolds decomposition, the Navier Stokes equation Equation 2.11 can be rewritten by decomposing velocity, stress and strain, then averaging all terms over a enough long time T:

$$U_j \frac{\partial U_i}{\partial x_j} + \overline{u_j \frac{\partial u_j}{\partial x_j}} = \frac{1}{\rho}\frac{\partial}{\partial x_j}\left(\Sigma_{ij}\right) \tag{2.15}$$

$$\Sigma_{ij} = -P\delta_{ij} + 2\mu S_{ij} \tag{2.16}$$

where Σ_{ij} is the mean stress tensor, P is the mean pressure and S_{ij} is the mean strain tensor. In order to solve the turbulence, we need to simplify the second term on the left hand side.

Recall the continuity equation Equation 2.13

$$\frac{\partial \tilde{U}_i}{\partial x_i} = 0 \tag{2.17}$$

with Equation 2.12, the continuity equation is decomposed

$$\frac{\partial \tilde{U}_i}{\partial x_i} = \frac{\partial}{\partial x}\left(U_i + u_i\right) = \frac{\partial U_i}{\partial x_i} + \frac{\partial u_i}{\partial x_i} = 0 \tag{2.18}$$

if we average the continuity equation for an enough long time T, the fluctuating term in Equation 2.18 becomes zero

$$\overline{\frac{\partial u_i}{\partial x_i}} = \frac{\partial}{\partial x_i}(\overline{u_i}) = 0 \tag{2.19}$$

the continuity equation is simplified to

$$\overline{\frac{\partial \tilde{U}_i}{\partial x_i}} = \overline{\frac{\partial U_i}{\partial x_i}} + \overline{\frac{\partial u_i}{\partial x_i}} = \frac{\partial_i}{\partial x_i}(\overline{U_i}) = \frac{\partial U_i}{\partial x_i} = 0 \tag{2.20}$$

Return to Equation 2.15, the second term can be also expressed by

$$\overline{u_j \frac{\partial u_i}{\partial x_j}} = \frac{\partial}{\partial x_j}\overline{u_i u_j} - \overline{u_i \frac{\partial u_j}{\partial x_j}} \tag{2.21}$$

According to Equation 2.19, the second term on the left hand side equals to zero

$$\overline{u_j \frac{\partial u_i}{\partial x_j}} = \frac{\partial}{\partial x_j}\overline{u_i u_j} \tag{2.22}$$

Equation 2.22 represents the effect of convective transport of the mean momentum by fluctuation, it exchanges the momentum between mean flow and turbulence. Then the Reynolds averaged Navier Stokes (RANS) equation is obtained by substituting Equation 2.22 to Equation 2.15

$$U_j \frac{\partial U_i}{\partial x_j} + \frac{\partial \overline{u_j u_i}}{\partial x_j} = \frac{1}{\rho}\frac{\partial}{\partial x_j}\left(\Sigma_{ij}\right) \tag{2.23}$$

where Σ_{ij} is the mean stress tensor.

In Equation 2.23, Σ_{ij} represents the mean stress. Based on this assumption, we might assume the turbulent term $-\rho\overline{u_j u_i}$ to be also a type of stress. we can merge these two terms into the right hand side

$$U_j \frac{\partial U_i}{\partial x_j} = \frac{1}{\rho}\frac{\partial}{\partial x_j}\left(\Sigma_{ij} - \rho\overline{u_j u_i}\right) \tag{2.24}$$

The turbulent term is given a new name Reynolds stress τ_{ij}

$$\tau_{ij} = -\rho\overline{u_i u_j} \tag{2.25}$$

the Reynolds stress tensor is symmetric along the diagonal direction

$$\tau_{ij} = -\rho\overline{u_i u_j} = -\rho\overline{u_j u_i} = \tau_{ji} \tag{2.26}$$

The diagonal components of τ_{ij} are called normal Reynolds stress. They are $\rho\overline{u_1^2}$, $\rho\overline{u_2^2}$ and $\rho\overline{u_3^2}$. But the normal stress components have little effect on the transport of mean momentum, while the off-diagonal terms are dominant in the transport process.

2.6 Turbulent boundary layer

The total shear stress is the sum of mean shear stress Σ_{ij} and Reynolds stress $-\rho\overline{u_j u_i}$ in Equation 2.24. On the sea bed, the non-slip boundary condition requires turbulent flow velocity to decay to zero, as well as the Reynolds stress. Thus the viscous shear stress is the only component of shear stress left. If we consider a two dimensional flow and assign y axis to the normal to the sea bed, the wall shear stress τ_w can be expressed by

$$\tau_w = \rho\nu\left(\frac{dU}{dy}\right)_{y=0} \tag{2.27}$$

The frictional velocity u_τ is used to represent the wall shear stress

$$u_\tau = \sqrt{\frac{\tau_w}{\rho}} \tag{2.28}$$

Near the wall, viscosity dominates, which is in contrast to free shear flow where viscous force is negligible. Next we will find the boundary of viscous force domination and Reynolds stress domination for a turbulent boundary layer.

Two new variables, non-dimensional distance from the wall y^+ and non-dimensional mean velocity u^+, are denoted by frictional velocity

$$y^+ = \frac{u_\tau y}{\nu} \tag{2.29}$$

$$u^+ = \frac{U}{u_\tau} \tag{2.30}$$

The expression of y^+ is similar to a local Reynolds number. Its magnitude can be expected to determine the relative importance of viscous and turbulent stress. Thus different regions and layers are determined by the value of y^+

Prandtl (1925) proposed that at high Reynolds number near the wall, there is an inner layer in which the mean velocity profile is determined by the viscosity. Very close to the wall, the non-slip condition forces $U_i = 0$. If we apply the RANS equation near the wall, it produces

$$\frac{\partial}{\partial y}\left(\mu\frac{\partial U}{\partial y}\right) = \rho {u_\tau}^2 \tag{2.31}$$

Integrating Equation 2.31 over the thickness of turbulent boundary layer, we obtain

$$u^+ = y^+ \tag{2.32}$$

Equation 2.32 gives a linear relation between u^+ and y^+, and is only valid for small y^+. This linear inner layer is called viscous sublayer. Outside the viscous sublayer, there is an outer part of the inner layer for large y^+, which is called log law layer. Inside this layer, the profile of u^+ versus y^+ agrees well with logarithmic shape

$$u^+ = \frac{1}{\kappa}\ln y^+ + B \tag{2.33}$$

where B is constant, and κ is von Karman constant.

Figure 2.6 shows the profile of the turbulent inner layer based on the experiment. It is easy to find that the viscous sublayer is around $y^+ < 5$, and the log law corresponds with the experiment for $y^+ > 30$. In the simulation of high Reynolds number flow, the RANS model becomes unstable and inaccurate when it very close to the wall and it is convenient to apply the so-called wall function at the wall. The wall function simulates the velocity distribution inside the inner layer just as those illustrated above. Therefore, the first layer of grids in the numerical simulation should be placed at $y^+ > 30$ to avoid disturbance to the wall function.

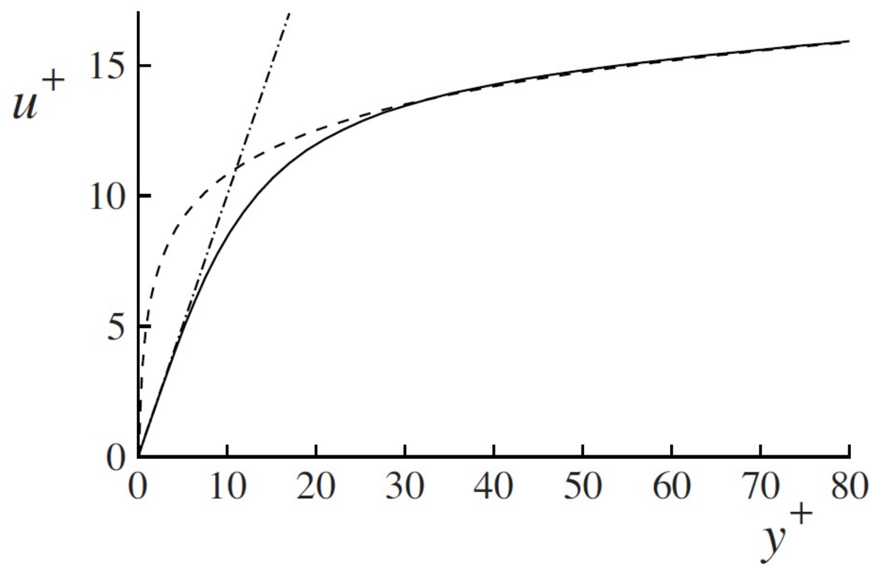

Figure 2.6: Near-wall profiles of mean velocity. solid line: DNS data of Kim et al. (1987), Re = 13,750; dot–dashed line: $u^+ = y^+$; dashed line: the log law(Pope (2001))

2.7 Eddy viscosity concept

By the Reynolds decomposition, turbulent velocity has been isolated. However, Equation 2.25 contains unknown variables such as P, U_i, and nine components of τ_{ij}, which exceeds the number of known equations (three RANS equations for mean flow plus one continuity equation). Hence, it is challenging to solve the RANS equations completely.

One concept is to replace the unknown averages of products of fluctuating quantities $\overline{u_i u_j}$ with mean velocity components. An algebraic relation or a set of transport equations that expresses such relation between the unknown Reynolds stress and the mean velocity components are called turbulence model.

$-\rho\overline{u_j u_i}$ has been assumed to be a special stress. Furthermore, we assume the expression of Reynolds stress is similar to the expression of viscous stress term Σ_{ij}, then Reynolds stress has following form:

$$\tau_{ij} = -\rho\overline{u_i u_i} = 2\rho\nu_T S_{ij} - \frac{2}{3}\delta_{ij} k\rho \tag{2.34}$$

where ν_T is turbulent or eddy-viscosity, k denotes the mean turbulent kinetic energy, defined as

$$k = \frac{1}{2}\overline{u_i u_i} \tag{2.35}$$

The second term of Equation 2.34 on the right hand side is to ensure the identity of relation

$$-\overline{u_i u_i} = -2k = 2\nu_T S_{ii} - \frac{2}{3}k\delta_{ii} \tag{2.36}$$

recovered when $i = j$. Equation 2.34 represents the so-called eddy viscosity concept, which is first proposed by Boussinesq (1877). If we introduce the eddy-viscosity back to Equation 2.24, it becomes

$$U_j \frac{\partial U_i}{\partial x_j} = -\frac{\partial}{\partial x_i}\left(\frac{P}{\rho} + \frac{2}{3}k\right) + \frac{\partial}{\partial x_j}\left[2\left(\nu + \nu_T\right) S_{ij}\right] \tag{2.37}$$

the total viscosity or effective viscosity becomes the sum of molecular viscosity and turbulent viscosity. Besides, for the second term on the right hand side, the turbulent kinetic energy k is a type of turbulent equivalence to the mean static pressure, if k is not treated as a dependent variable in the turbulence model, it can be easily absorbed by pressure P.

The application of eddy-viscosity relates the mean flow with turbulence, but an assumption or approximation for eddy-viscosity ν_T need to be found so that the total number of known equations equals the number of unknown variables. It is the choice of approximation for eddy-viscosity that distinguishes different turbulence models.

Depending on the number of differential equations except the partial differential equations for mean velocity field, turbulence models can be classified into three types: zero-equation models, one-equation models and two-equation models. Prandtl (1925) proposed that fluid would be transported a certain distance before it is fully mixed with surrounding water, as shown in Figure 2.7. Furthermore, based on this assumption, Prandtl decomposed the eddy viscosity into the resulting length scale multiplying velocity scale

$$\nu_T = l \cdot V \tag{2.38}$$

where l is the length scale, and V is the velocity scale. If in a turbulence model, both length scale and velocity scale are expressed by the mean flow through algebraic expressions, then the model is zero-equation model. Constant eddy-viscosity models and mixing length models are the typical zero-equation models; If the transport effect of length scale or velocity scale is considered in a turbulence models and one of the scales is expressed by transport equation

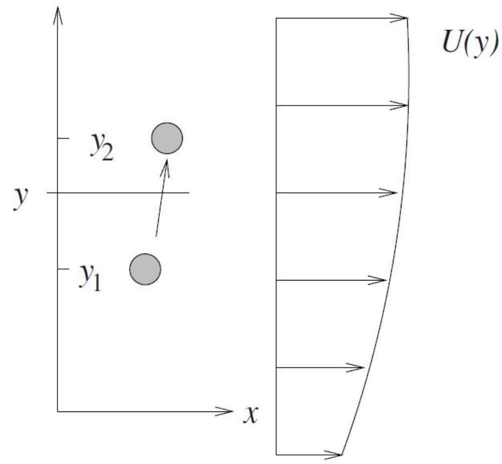

Figure 2.7: Profile of turbulent shear flow along the x-axis illustrating the random displacement of a fluid parcel by a distance for Prandtl mixing length theory.(Pozrikidis (2009)

(partial differential equation), then the model is classified as one-equation model, k- model belongs to one-equation models; If both transport effect of length scale and velocity scale are accounted in a turbulence model, then this model belongs to two-equation model, $k-\omega$ and $k-\epsilon$ models are the representative two-equation models.

In this study, standard $k-\omega$ two-equation model is applied, thus the details of this model is illustrated.

2.8 $k-\omega$ turbulence model

Using algebraic relations to express the length or the velocity scale has an instinctive defect, it assumes the turbulence is in a state of local equilibrium. However, the characteristic turbulent quantities (turbulent velocities and eddies) are transported after being generated. In two-equation models, both convective and diffusive transport of turbulence are considered.

Prandtl and Wieghardt (1947) and Kolmogorov (1942) independently suggested that the velocity scale should be equal to the square root of the mean turbulent kinetic energy

$$V = \sqrt{k} \tag{2.39}$$

Equation 2.38 becomes

$$\nu_T = \sqrt{k}L \tag{2.40}$$

Eq (2.40) is called Prandtl-Kolmogorov relation, where L is the length scale. Most of the two-equation models are based on the Prandtl-Kolmogorov relation.

Subsequently, the transport equations of the mean turbulent kinetic energy k and the length scale L need to be formulated to make the model closure. The transport equation for k is derived from the turbulent Navier Stokes equation with $\overline{u_i}$ multiplied on both sides

$$\frac{\partial k}{\partial t} + U_j \frac{\partial k}{\partial x_j} = -\overline{u_i u_j}\frac{\partial U_i}{\partial x_j} - 2\nu\overline{s_{ij}s_{ij}} - \frac{\partial}{\partial x_i}\left[\overline{u_i\left(\frac{p}{\rho} + k\right)}\right] + \frac{\partial}{\partial x_i}2\nu\left(\overline{u_j s_{ij}}\right) \tag{2.41}$$

Equation 2.41 is rewritten

$$\frac{\partial k}{\partial t} + U_j \frac{\partial k}{\partial x_j} = P_k - \epsilon + D_k \tag{2.42}$$

where

$$P_k = -\overline{u_i u_j}\frac{\partial U_i}{\partial x_j} \tag{2.43}$$

$$\epsilon = 2\nu\overline{s_{ij}s_{ij}} \tag{2.44}$$

$$D_k = -\frac{\partial}{\partial x_i}\left[\overline{u_i\left(\frac{p}{\rho} + k\right)}\right] + \frac{\partial}{\partial x_i}2\nu\left(\overline{u_j s_{ij}}\right) \tag{2.45}$$

where the s_{ij} is turbulent stress tensor. P_k is a production term, and represents the production of work of turbulent kinetic energy created by the interaction of the mean flow and the turbulent stresses; D_k is a diffusion term, and represents the diffusion of turbulent kinetic energy due to turbulent and molecular transport; ϵ is the dissipation term, and represents the viscous dissipation rate of the turbulent kinetic energy. These three terms are simplified by the so-called eddy-viscosity concept, in order to be consistent with RANS equation. The production term P_k

has Reynolds stress in its expression and can be modelled by the eddy-viscosity assumption

$$
\begin{aligned}
P_k &= \left(2\nu_T S_{ij} - \frac{2}{3}\delta_{ij} k\right)\frac{\partial U_i}{\partial x_j} \\
&= 2\nu_T S_{ij}\frac{\partial U_i}{\partial x_j} - \frac{2}{3}k\frac{\partial U_i}{\partial x_i}
\end{aligned}
\tag{2.46}
$$

Incompressible flow has been assumed, thus the second term on the right hand side vanishes. The final expression for the production term is

$$
P_k = 2\nu_T S_{ij}\frac{\partial U_i}{\partial x_j} \tag{2.47}
$$

The diffusion term in Equation 2.45 is approximated by the gradient of mean diffusive transport of k.

$$
-\overline{u_i\left(k + \frac{p}{\rho}\right)} \approx (\nu + \gamma_k)\frac{\partial k}{\partial x_i} \tag{2.48}
$$

where γ_k is diffusivity of turbulent kinetic energy. A new dimensionless diffusion number σ_k is defined

$$
\sigma_k = \frac{\nu_T}{\gamma_k} \tag{2.49}
$$

By substituting Equation 2.48 and Equation 2.49 to Equation 2.45, the final expression for diffusive term D_k is obtained

$$
D_k = \frac{\partial}{\partial x_i}\left(\nu + \frac{\nu_T}{\sigma_k}\frac{\partial k}{\partial x_i}\right) \tag{2.50}
$$

For the dissipation term ϵ, the $k-\omega$ model (Wilcox (1988)) introduces a new parameter of specific dissipation rate ω by dimension analysis

$$
\epsilon \approx \frac{V^3}{L} = \beta_k k\omega \tag{2.51}
$$

where β_k is closure coefficient for the turbulent kinetic energy transport equation. Through Equation 2.51, the length scale can be derived

$$
L = \frac{\sqrt{k}}{\omega} \tag{2.52}
$$

The eddy-viscosity in Equation 2.40 is modified by

$$\nu_T = \frac{k}{\omega} \tag{2.53}$$

The final expression for the turbulent kinetic energy transport equation is

$$\frac{\partial k}{\partial t} + U_j \frac{\partial k}{\partial x_j} = 2\nu_T S_{ij} \frac{\partial U_i}{\partial x_j} + \frac{\partial}{\partial x_j}\left[\left(\nu + \frac{\nu_T}{\sigma_k}\right)\frac{\partial k}{\partial x_j}\right] - \beta_k k\omega \tag{2.54}$$

By the same process, the transport equation for specific dissipation rate ω is

$$\frac{\partial \omega}{\partial t} + U_j \frac{\partial \omega}{\partial x_j} = 2\nu_T S_{ij} \frac{\partial U_i}{\partial x_j} + \frac{\partial}{\partial x_j}\left[\left(\nu + \frac{\nu_T}{\sigma_\omega}\right)\frac{\partial \omega}{\partial x_j}\right] - \beta_\omega \omega^2 \tag{2.55}$$

where σ_ω and β_ω are closure coefficients for the transport equation of specific dissipation rate. Combining Equation 2.37, Equation 2.54 and Equation 2.55, the model system is closed. The mean velocities and pressure can be solved by numerical methods.

Chapter 3

Numerical method

This chapter gives an introduction to CFD, numerical method used by OpenFOAM and how the differential equations in chap.2 are numerically solved. The finite volume method, OpenFOAM and SIMPLE algorithm are briefly described.

3.1 Computational Fluid Dynamics (CFD)

Flow field can be described by a set of partial differential equations. Analytical solution to these equations is impossible to obtain in most cases. For this reason, Computational Fluid Dynamics (CFD) is applied to obtain an approximate numerical solution. CFD discretizes the partial differential equations to a set of simple algebraic equations, which can be solved on a computer. The flow field is divided into many small domains both in space and in time, and the discretization is applied to every small domains. Thus, an approximate numerical solution is obtained for each small domain and integrals over the small domains results the continuous solution of the flow field.

The components of numerical method are listed below (Ferziger and Peric (2012)):

- Mathematical Model
- Discretization Method
- Coordinate and basis vector system

- Numerical grid
- Finite approximation
- Solution method
- Convergence criteria

The idea is to illustrate some of the main components of numerical method inside the CFD software OpenFOAM, which is applied in this study.

3.2 OpenFOAM

OpenFOAM is a free, open source software for computational fluid dynamics, developed primarily by CFD Direct, on behalf of the OpenFOAM Foundation.

General Public License (GPL) gives users the freedom to modify and redistribute the software and a guarantee of continued free use — as long as the terms of the GPL are adhered to. Such a license is of the highest importance to the users, it enables the tookit to be used as a common platform, the development and implementation of innovative methods is stimulated.

OpenFOAM has an extensive range of features and is used heavily across most areas of engineering and science, by commercial and academic organisations(Greenshields (2015)).

OpenFOAM is a highly integrated software, it contains modules that cover all components of numerical method. The main modulus of OpenFOAM includes mesh tools, solvers and post-processor. The function of mesh tools is to build model, then mesh the whole calculation field, the resulting numerical grids should small enough to capture the smallest flow motion. blockMesh and snappyHexMesh are two built-in mesh tools in OpenFOAM.

Solvers are designated to specific flow situations. For example, potential flow needs to be solved by potentialFoam, turbulent flow is suitable to be solved by simpleFoam in steady-state and pisoFoam in transient state. In the present study, the flow is steady-state and turbulent, thus steady-state solver simpleFoam is chosen to be applied. This solver has been validated by Peralta et al. (2014), and it was shown that reproduces accurate solution for flow over complex 3D terrain.

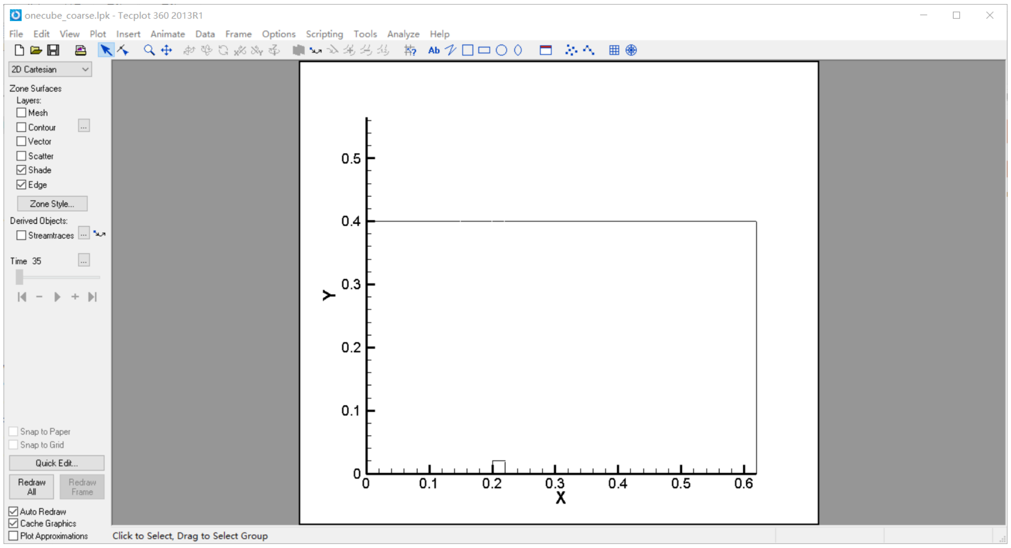

Figure 3.1: The interface of Tecplot

Post-processor is responsible for visualizing the results of the simulation. Tecplot is used in the post-processing, it can produce streamlines, contours and ect. (see Figure 3.1).

In the present study, OpenFOAM version is 2.4 and Tecplot 2013 version is used. System version is Ubuntu 14.04.

3.3 Finite volume method

The most important component that determines the accuracy of numerical method is a discretization method. Because OpenFOAM is based on the finite volume method, this section tends to give a brief introduction to the finite volume method.

In the finite volume method, the domain is subdivided into a finite number of small Control Volumes (CVs) by grids. The approach is to define CVs by a suitable grid and assign the computational node to the CV center, as shown in Figure 3.2. If we consider the generic conservation equation for a quantity ϕ and assume that the velocity field and all fluid proprieties are known, the integral form of the conservation equation in the finite volume method over CV volume Ω is expressed by

$$\int_S \rho\phi v \cdot n dS = \int_S \Gamma grad\phi \cdot n dS + \int_\Omega q_\phi d\Omega \tag{3.1}$$

where q_ϕ is the inner density change of ϕ. Equation 3.1 is applied to each CV, as well as to

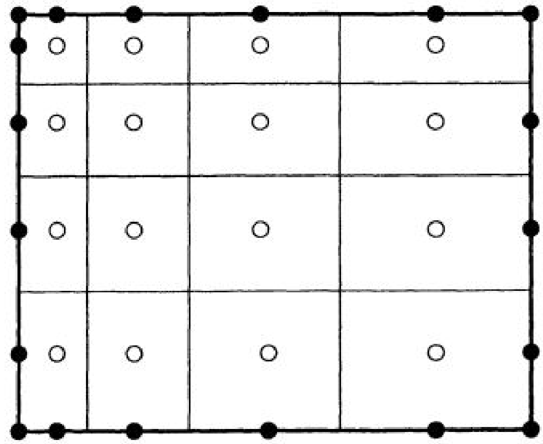

Figure 3.2: illustration of CV in the finite volume method (Ferziger and Peric (2012))

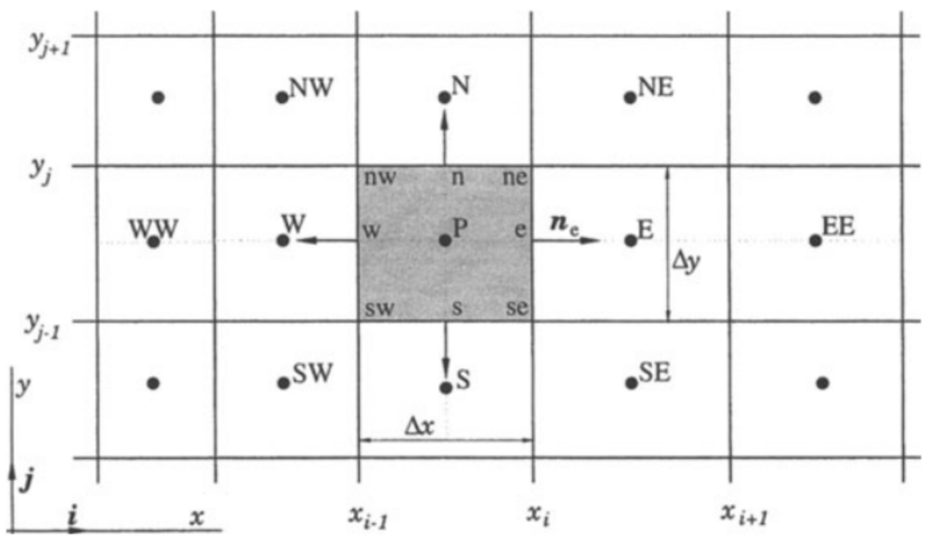

Figure 3.3: A typical CV and the notations used for a Cartesian 2D grid(Ferziger and Peric (2012))

the whole domain. If we sum up the equations for all CVs, we obtain the global conservation equation, because the surface integrals over inner CV faces cancel out. In Figure 3.3, a typical 2D CV is shown, the CV surface consists of four plane faces with lower-case letters denoting their direction, e(ease), w(west), n(north), s, (south). The integrals in the first two terms of Equation 3.1 over CV correspond to the net flux through the boundaries of CV, which is the sum of integrals over the four faces

$$\int_S f dS = \sum_k \int_{S_k} f dS \tag{3.2}$$

where f is the component of the convective or diffusive vector that normal to CV faces.

To calculate the integrals over CV in Equation 3.2, the value of f needs to be obtained for points along the surface. However, only the value at the CV center is calculated in the finite volume method, the values at other points should be approximated through the known points. The approximation lies on the cell-face values. The integral over one cell-face is approximated by values at one or several points on the cell-face. Then the net flux through all boundaries of CV equal to the sum of these values. One of the simplest approximation method is the midpoint rule: the cell-face values are approximated as a product of the integrand at cell-face center. Another approximation method is the trapezoid rule, in which the cell-face value is approximated at the face corners. In addition, there are also high-order approximations where the flux is evaluated at more than two locations, which gives higher accuracy of the surface integrals but also requires more computational resources.

Beside surface integrals, some terms in the transport equations require integrals over the CV volume. Similar to the approximation of surface integrals, the volume integral can be replaced by interpolating values of nodal points and using shape functions.

Both in the approximation of surface integrals and volume integrals, the values of quantities at the points (nodal points or cell-face center) are required. We have illustrated how to use these values to approximate the integrals along surface and volume, but the values of the points itself need to be interpolated, since only the value at cell-center is known in the finite volume method. Some frequently used schemes are listed below:

- Upwind Interpolation (UDS) approximates the values at cell-face by a back-difference or forward-difference approximation for the first derivative at the upstream node of that cell-face. UDS is the only approximation method that satisfies the boundedness criterion unconditionally.

- Linear Interpolation (CDS) is a straightforward approximation for the calculation of value at CV center that is to linearly interpolate the values between two nearest nodes. For example, in Figure 3.3, the value at location 'e' can be linearly interpolated by the values at nearest CV centers 'P' and 'E'. This is the simplest scheme and is the most widely used one.

- Quadratic Upwind Interpolation (QUICK)is similar to the linear interpolation, QUICK also approximates the values of points by interpolation through the nearest nodes, but the shape function of this method is parabolic rather then linear. A parabola requires a third points except the two nearest nodes, and the third point is taken on the upstream direction of the flow. In general, the third point is the second upstream node. Taking Figure 3.3 for example, if the flow direction is from 'P' to 'E', then the value at 'e' is approximated by a parabolic shape function using nodal values at 'P', 'E' and 'EE'. This scheme is more complex and accurate than the CDS scheme since one more node is accounted.

Except the schemes listed above, lots of other approximations have been proposed, e.g. linear Upwind Scheme (LUDS), which uses two successive upstream nodes to linearly interpolate the values on cell-face; Skew Upwind Scheme (SUS), which extrapolates the values along a streamline to the upwind direction. These schemes are complex and difficult to programming, thus they are not widely accepted as the general schemes.

3.4 The solution method

We have introduced the discretization methods that discretize the calculation field into separated CVs and the approximation to field values of CV by the values at the grid nodes (The CV center in the finite volume method). But the problem is how we solve the differential equations at the grid nodes, and how the solution method is determined. In the present study, velocity and pressure are the two main flow variables. The Navier Stokes equations are the basic equations to obtain velocities and pressure of the field. RANS equations can be also considered to be an extension of the NS equations. Besides, $k-\omega$ turbulence model , which is applied in this study has a similar set of partial differential equations as the NS equations. Thus, if the NS equations are solved and differential equations in turbulence model can be solved in the same way.

In general, starting with a guessed velocity field, we can solve the NS equations iteratively to arrive at the converged solution for the velocity components. The real difficulty is to obtain the pressure field. The pressure gradient in the NS equations serves as a sort of source term and there is no explicit equation to obtain it. However, the pressure is indirectly related to the continuity equation. When the "correct" pressure is substituted into the NS equation, the resulting velocity field should satisfy the continuity equation. This implies implicitly that pressure can be determined by other numerical iterations.

3.4.1 Discretiztion equations for two dimensions

At first, we list the governing equations for the flow field without turbulence.

The continuity equation is

$$\frac{\partial \rho}{\partial t}+\frac{\partial}{\partial x_j}\left(\rho u_j\right)=0 \tag{3.3}$$

and the Navier Stokes equation is

$$\rho\frac{\partial}{\partial t}\left(u_i\right)+\rho u_j\frac{\partial}{\partial x_j}\left(u_i\right)=\underbrace{-\frac{\partial p}{\partial x_i}}_{S}+\frac{\partial}{\partial x_j}\left(\mu\frac{\partial u_i}{\partial x_j}\right) \tag{3.4}$$

Here u_i, u_j represent the velocities of flow without turbulence, and S is called the source term.

Let us consider a two dimensional flow situation. The two dimensional form of Equation 3.4 can be written as

$$\rho\frac{\partial}{\partial t}\left(u_i\right)+\frac{\partial}{\partial x}\left(J_x\right)+\frac{\partial}{\partial y}\left(J_y\right)=S \tag{3.5}$$

where J_x and J_y are the total (convection and diffusion) momentum fluxes which are defined by

$$J_x=\rho u\cdot u_i-\mu\frac{\partial u_i}{\partial x} \tag{3.6}$$

$$J_y=\rho v\cdot u_i-\mu\frac{\partial u_i}{\partial y} \tag{3.7}$$

If we try to construct the discretization form of the Navier Stokes equations, the representation of velocity and pressure gradient integrated over the CV need to be specified. We concentrate on a CV at point P in Figure 3.4. The integrals of pressure gradient $-\partial p/\partial x$ can be expressed as

$$p_w-p_e=\frac{p_W+p_P}{2}-\frac{p_P+p_E}{2}=\frac{p_w-p_E}{2} \tag{3.8}$$

where the pressures p_W and p_P with subscripts represent the values at the points defined in Figure 3.3. If we consider a simple one dimensional flow, the gradient of velocity $\partial u/\partial t$ is

$$u_e-u_w=\frac{u_P+u_E}{2}-\frac{u_W+u_P}{2} \tag{3.9}$$

where the velocities with subscripts represent the values at the points in Figure 3.3.

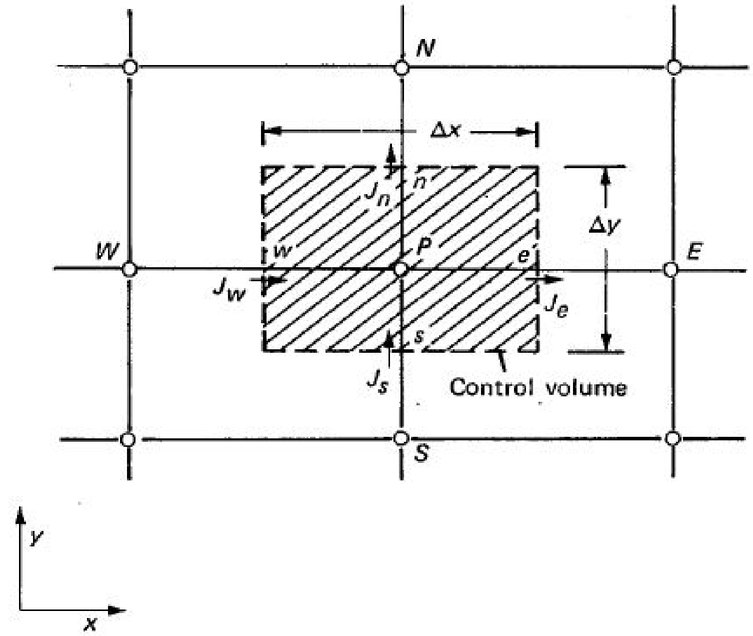

Figure 3.4: CV in two-dimensional (Patankar (1980))

Now the integrals of Equation 3.5 over the CV shown in Figure 3.4 gives the discretization equation as follow

$$\frac{\left(\rho_P u_P - {\rho_P}^0 {u_P}^0\right)\Delta x \Delta y}{\Delta t} + J_e - J_w + J_n - J_s = (S_C + S_P u_P)\,\Delta x \Delta y \tag{3.10}$$

where u_P is the velocity vector at point P, and the source term S has been linearized in the usual manner by S_C and S_P. ρ_P and u_P are assumed to be prevail over the whole CV. The "old" values (the values at the beginning of a time step/iteration) are denoted by ${\rho_P}^0$ and ${u_P}^0$. The other terms are called "new" value (the values at the end of a time step/iterations). J_e, J_w, J_n and J_s are the integrated total fluxes over the CV faces at different directions.

Similarly, the continuity equation Equation 3.3 can be integrated to obtain

$$\frac{\left(\rho_P - {\rho_P}^0\right)\Delta x \Delta y}{\Delta t} + F_e - F_w + F_n - F_s = 0 \tag{3.11}$$

where F_e, F_w, F_n and F_s are the mass flow rates through the boundary faces of CV. If velocity prevails over the surfaces at e, w, n and s, then the mass flow rates are simplified to

$$\begin{aligned} F_e &= \left(\rho u\right)_e \Delta y \\ F_w &= \left(\rho u\right)_w \Delta y \\ F_n &= \left(\rho v\right)_n \Delta x \\ F_s &= \left(\rho v\right)_s \Delta x \end{aligned} \tag{3.12}$$

Then we multiply Equation 3.11 by u_P and subtract it from Equation 3.10, it is obtained

$$\begin{aligned} &\left(u_P - u_P^0\right) \frac{\rho_P^0 \Delta x \Delta y}{\Delta t} + (J_e - F_e u_P) - (J_w - F_w u_P) + (J_n - F_n u_P) \\ &- (J_s - F_s u_P) = (S_C + S_P u_P)\Delta x \Delta y \end{aligned} \tag{3.13}$$

Now we need some special treatments to the total momentum fluxes J. We define a new parameter J^* that is the function of J

$$J^* = \frac{J\delta}{\mu} = P_e u - \frac{\partial u_i}{\partial\left(x/\delta\right)} \tag{3.14}$$

where P_e is the Peclet number, which equals to $\frac{\rho u \delta}{\mu}$. δ is the distance between grids shown in Figure 3.5. In two dimensions, δ has values in four directions 'e', 'w', 'n' and 's'. The first term on the right hand side is the value of u at the interface between grids, which equals to some weighted average values of its neighbouring grids; The second term is the gradient of velocity and is some multiple to subtraction of values at neighbouring grids. Thus Equation 3.14 becomes

$$J^* = P\left[\alpha 1 u_n + (1-\alpha 1) u_{n+1}\right] - \beta(u_n - u_{n+1}) \tag{3.15}$$

where $\alpha 1$ is constant coefficient, and u_n and u_{n+1} are the velocity vectors at grid n and $n+1$ as shown in Figure 3.5. In a simplified manner, J^* is expressed as

$$J^* = B^* u_n - A^* u_{n+1} \tag{3.16}$$

where B^* and A^* are dimensionless coefficients that depend on the Peclet number P.

Now back to Equation 3.13, Equation 3.16 provides a way to express terms such as $J_w - F_w u_P$ to be

$$J_w - F_w u_P = a_E\left(u_P - u_E\right) \tag{3.17}$$

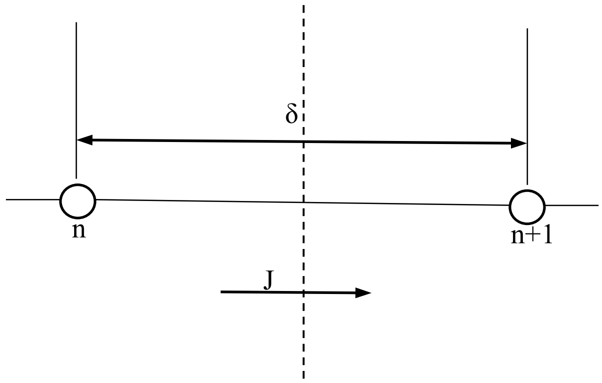

Figure 3.5: Total flux at interface

Similarly, other terms in Equation 3.13 can be rewritten in the same way. After rearranging the equation, the two-dimensional discretization equation becomes

$$a_P u_P = a_E u_E + a_W u_W + a_N u_N + a_S u_S + b \tag{3.18}$$

where a_E, a_W, a_N and a_S are dimensionless coefficients that depend on the value of Peclet number and velocity at the points denoted by the subscripts. a_P and b are defined by

$$a_P = a_E + a_W + a_N + a_S + a_p^0 - S_P \Delta x \Delta y \tag{3.19}$$

$$b = S_C \Delta x \Delta y + a_P^0 u_P^0 \tag{3.20}$$

Here $a^0{}_P$ refer to the known value a_P at the beginning of a time step/iteration.

3.4.2 The SIMPLE algorithm

We rewrite Equation 3.18 and isolate the pressure gradient from the source terms S_C and S_P

$$a_P u_P = a_W u_W + a_E u_E + a_N u_N + a_S u_S + b + (\delta p) A_s \tag{3.21}$$

where δp is the difference of pressure and A_s is area coefficient that depends on the direction of velocity.

To solve this equation, we need to guess a set of pressure field: p_P^*, p_W^*, p_E^*, p_N^* and p_S^* (At the beginning of a simulation, these values are the initial values of the internal field and the boundary conditions), then the guessed pressure field should be substituted to the discretization functions to obtain velocities. In two dimensions, the discretization functions are

$$\begin{aligned} a_P u_P &= a_W u_W + a_E u_E + a_N u_N + a_S u_S + b + \left(p_W - p_E\right) A_{xs} \\ a_P v_P &= a_W v_W + a_E v_E + a_N v_N + a_S v_S + b + \left(p_S - p_N\right) A_{ys} \end{aligned} \tag{3.22}$$

Then the velocity components u^* and v^* at each grid point can be solved. However, the solution is not accurate, it normally does not satisfy the continuity equation. Thus, we further assume corrections to both pressure and velocity

$$p = p^* + p^{'} \tag{3.23}$$

$$\begin{aligned} u &= u^* + u^{'} \\ v &= v^* + v^{'} \end{aligned} \tag{3.24}$$

The pressure correction is calculated by

$$a_p p_P^{'} = a_E p_E^{'} + a_W p_W^{'} + a_N p_W^{'} + a_S p_N^{'} + a_T p_T^{'} + a_B p_B^{'} + b \tag{3.25}$$

All coefficients in Equation 3.25 can be calculated through guessed velocity field and pressure field. Thus the pressure correction is obtained from Equation 3.25. $p^{'}$ is calculated for all grids and is substituted into Equation 3.22 to obtain velocity correction $u^{'} = f(p^{'})$ and $v^{'} = g(p^{'})$. The updated velocity $u = u^* + f(p^{'})$ and $v = v^* + g(p^{'})$ are again substituted back to the continuity equation Equation 3.11 to solve pressure correction $p^{'}$ and velocities u, v. Then the corrected pressure p is treated as a new guessed pressure field and the above calculation steps are repeated until the final correction terms $p^{'}$ and $u^{'}$ are smaller than the tolerance. In general, after two or three iterations, the solution should be convergent.

After the NS equations are solved, the k- equation and ω- equation can be solved by the same procedures.

The above illustrated solution method is called Semi-Implicit Method for Pressure-Linked Equations (SIMPLE), which is the kernel algorithm in the OpenFOAM solver simpleFoam.

In summary, the important operations, in order to apply the SIMPLE algorithm properly, are:

1. Guess the pressure field p^*.
2. Solve the momentum equations Equation 3.22, to obtain u^* and v^*.
3. solve the equation of $p^{'}$ and Substitute it into Equation 3.22 to obtain velocity correction $u^{'}$ and $v^{'}$
4. Calculate p from Equation 3.23 by adding $p^{'}$ to p^*.
5. Calculate u and v from Equation 3.24.
6. Solve the discretization equations for other quantities, such as mean turbulent kinetic energy k and the specific dissipation rate ω if they influence the flow field through source term or dissipation term.
7. Treat the corrected pressure p as a new guessed pressure p^* , repeat the step 2 to 7 until a converged solution is obtained.

Chapter 4

Numerical set-up

This chapter gives detailed descriptions of domain, mesh, solver, flow conditions and boundary conditions that are applied in the simulation. The numerical set-up includes two simulations, the flow around one square cylinder and the flow around two square cylinders with different intervals. Most of the numerical setups are generic for both simulations.

4.1 Numerical domain

Numerical domain is an area or volume to restrict the extension of simulation. The domain is vital to the accuracy of the solution: a too small domain is not able to capture the necessary details of the flow. For instance, if we simulate flow around a circular cylinder, the circular cylinder would alter ambient flow behaviors. The velocity and pressure field surrounding the cylinder would exhibit unique distributions. In return, the altered velocity field and pressure field also impose forces on the cylinder, and the spatial differences in velocity and pressure generate viscous force and pressure drag on the cylinder. These forces are sensitive to the domain size, because the domain must include every variation of flow properties that could affect the drag and lift force. Therefore, the domain must be chosen with great care. A common way to find a suitable domain is the domain size convergence test, in which a set of successively increasing domain sizes are tested, until an optimal domain size is found. For this domain, the solution should be domain-independent.

Depending on the simulation, the domain sizes are not uniform in all directions. The opti-

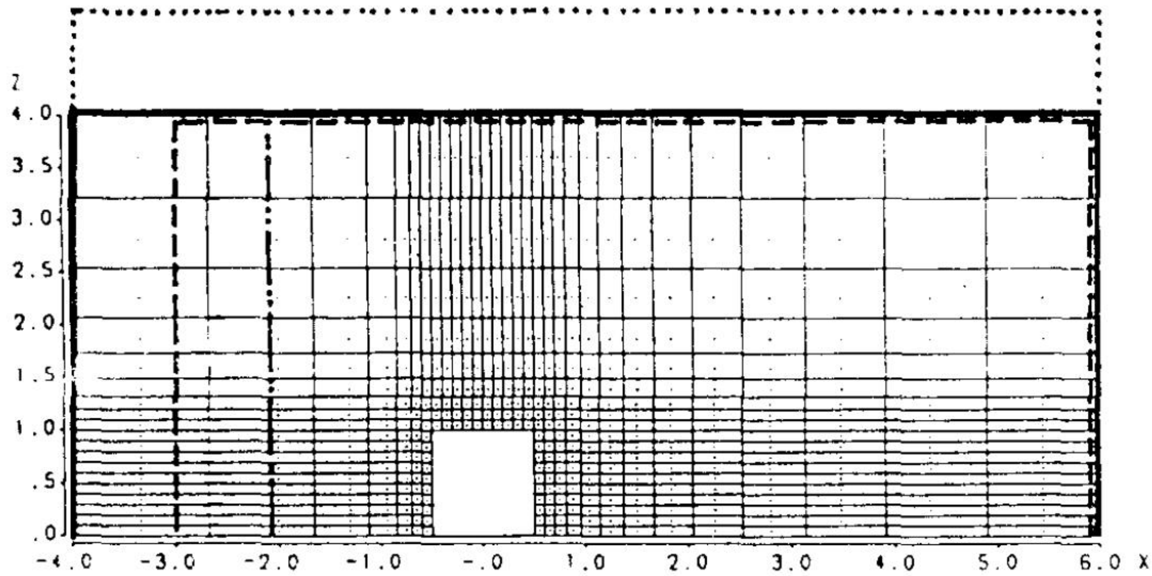

Figure 4.1: Convergence test of computational domain (Baetke et al. (1990))

mal domain length in upstream and downstream directions are normally different, as well as in transverse directions. In general, vortices are generated at the downstream side of an obstacle, these vortices extend to further downstream than the variation of flow at the upstream, which means a longer downstream length is required for the domain.

Apart from the domain size convergence test, a convenient way is to find similar flow problems or convergence tests with reference to their setup of domain. Tian et al. (2013) simulated flow around a rectangular cylinder with different aspect ratios. He defined a domain with ten times of the cylinder length from the inlet to the center of cylinder and 25 times of cylinder length in downstream direction, while the crosswise width is twenty times of cylinder length. Baetke et al. (1990) has conducted domain size convergence test for flow over surface-mounted obstacles, his results has demonstrated that if the ratios of domain sizes to dimension of obstacle in three directions are larger than those shown in Figure 4.1, the significant influence of domain size on the pressure distribution is eliminated. Furthermore, the simulation of flow around a two-dimensional block by Cheng and Porté-Agel (2013) has a similar model and flow conditions to the present study. He defined domain sizes with five times of block height in upstream, 17 times of block height in downstream and ten times of block height in transverse relative to the block center.

In the present study, domain configurations for the one cylinder simulation is defined in

Figure 4.2: Definition of domain for the simulation of one square cylinder

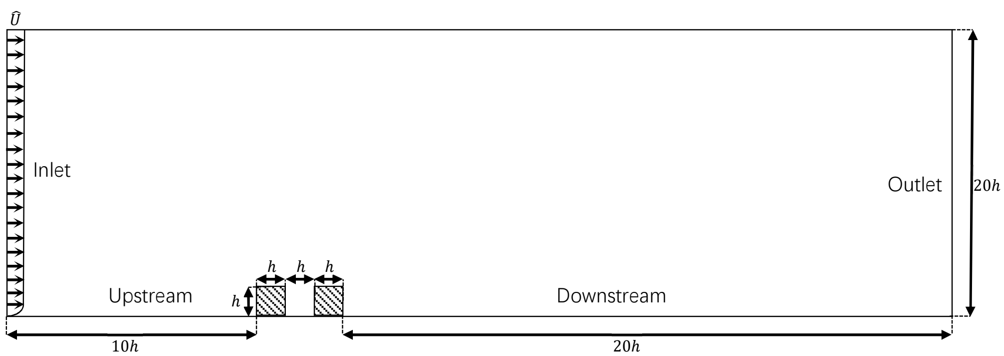

Figure 4.3: Definition of domain for the simulation of two square cylinders with interval $L = h$

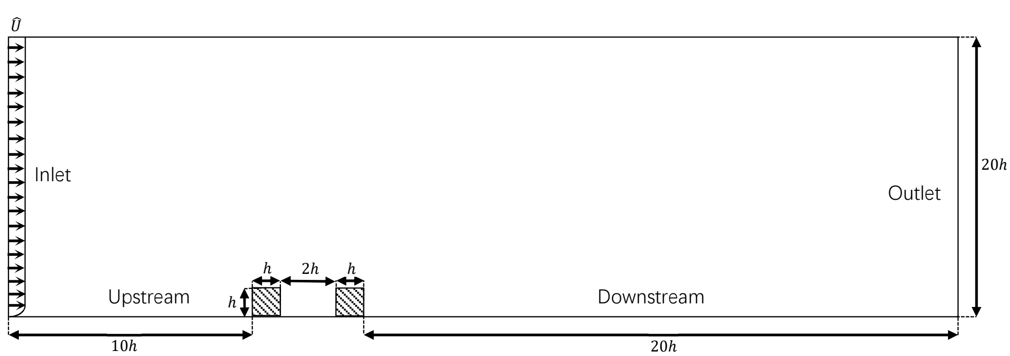

Figure 4.4: Definition of domain for the simulation of two square cylinders with interval $L = 2h$

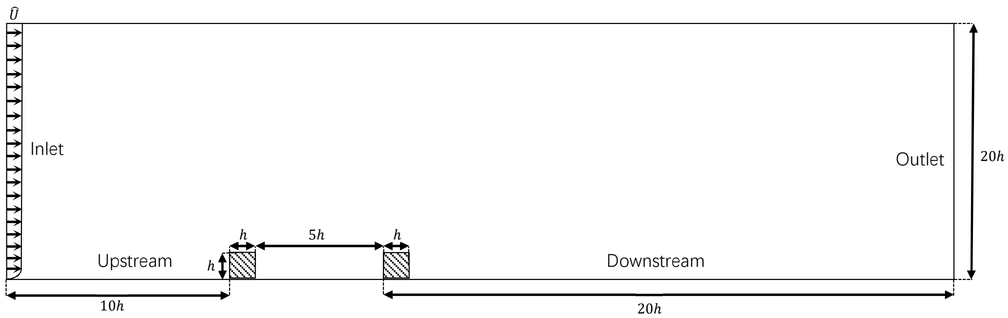

Figure 4.5: Definition of domain for the simulation of two square cylinders with interval $L = 5h$

Table 4.1: Geometrical parameters

Name	Parameter	Unit	Value(s)
Height of the cylinder	h	m	0.02
Uniform inflow velocity	$\hat{U}$	m/s	0.2
Upstream length	L_u	m	0.2
Downstream length	L_d	m	0.4
Height of the domain	H_D	m	0.4
Interval	L	m	$h, 2h, 5h$

Figure 4.2, and the main geometric parameters are listed in Table 4.1. The distance from the inlet to the front face of the cylinder L_u is set to be $10h$, the distance from the rear face of the cylinder downward to the outlet L_d is defined to be $20h$ and the height of domain H_D is taken to be $20h$ in order to eliminate any far-field effects. These dimensional parameters are larger than most of the similar simulations, and it ensure the domain size independence of the solution. Similar setups are applied to the simulation of two square cylinders, and the domains are defined in Figure 4.3, Figure 4.4 and Figure 4.5 for interval $L = h, 2h$ and $5h$.

4.2 Mesh set-up

The discretization of the domain results in a mesh, on which a set of the conservation equations is solved. Thus, the resulting cells or elements should be non-overlapping and fill all of the computational field. To satisfy this requirement, a variety of meshes have been proposed. Their structures, orthogonality, blocks, cell shapes and variable arrangements are different. but except the geometry of mesh, additional information about topology of the mesh is required, the topology includes element to element relations, face to element relations, element center and the values of volume/area. These parameters are important in the discretization equations.

In general, a geometric domain can be discretized by a structured or unstructured grid system. Structured grids are defined by their local indices(i, j, k), as shown in Figure 4.6. Structured

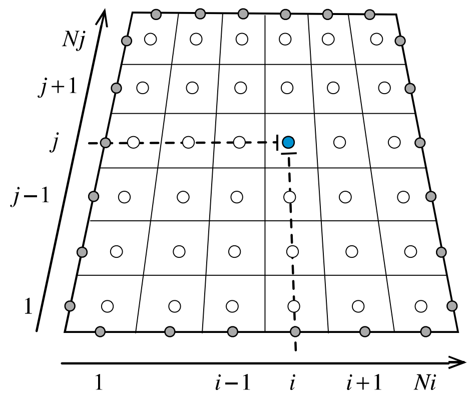

Figure 4.6: Indices and topology definition of structured grid(Moukalled et al. (2016))

grid has advantages in coding and efficiency, but it is limited by the geometries of obstacle and domain. Anther way to generate mesh is to adopt unstructured grid, which overcomes the deficiency of structured grid in geometric limitation. But it requires explicit topological information and consumes additional complexity (see Figure 4.7). For the present study, the cylinder and do-

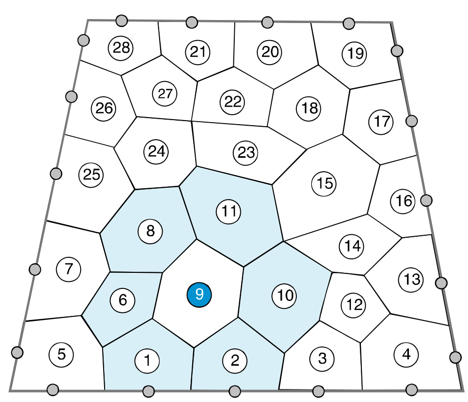

Figure 4.7: Unstructured grid mesh indexing(Moukalled et al. (2016))

main are simple and regular geometries, structured grid can produce a pretty accurate solution.

In OpenFOAM, blockMesh is applied to mesh the domain, and blockMesh relies on the partition of blocks. At first, the whole domain is divided into multiple blocks. Inside each block, mesh grids are independently created and stretched, but the number of elements must be consistent across the boundaries of blocks. In principal, the mesh grids around the zones of interest should be condensed and it should gradually scatter the grid when it moves away from the zones of interest. In this study, we focus on the flow phenomena when the flow hits the cylinder and the generation of vortices afterwards. Therefore, we assign many small blocks around the cylinder and less blocks with large area far away from it, as shown in Figure 4.8.

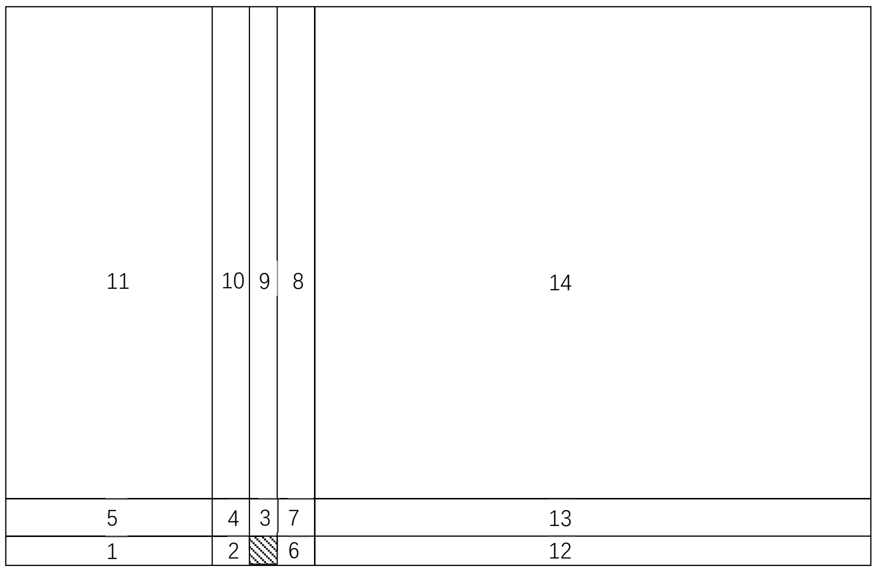

Figure 4.8: Blocks partition for the simulation of the one cylinder simulaton

In order to obtain a high quality solution, a fine mesh is applied at the blocks surrounding the cylinder, which is $No.2,3,4,6,7$ in Figure 4.8. These blocks have the same level of resolution and no internal stretch. The same strategy of block partition is applied to the simulation of two cylinders, as shown in Figure 4.9. The blocks No. 6,7 are defined to have the same high level of resolution as other blocks that surrounding the cylinders. As it is expected that the interaction between the two cylinders would produce many vortices with small scales, these phenomenons need to be fully captured with a sufficiently fine mesh. Besides, OpenFOAM is based on the finite volume method, so it only supports three-dimensional domains. The present two-dimensional simulation can be achieved by setting the faces in one-direction to be type of 'default'. Then OpenFOAM wouldn't account any quantities and variation in this direction, and the simulation degenerates to two-dimensional.

In order to produce a high quality mesh, skewness, mesh non-orthogonality and aspect ratio of the mesh need to be checked. These properties are the main factors in OpenFOAM that can

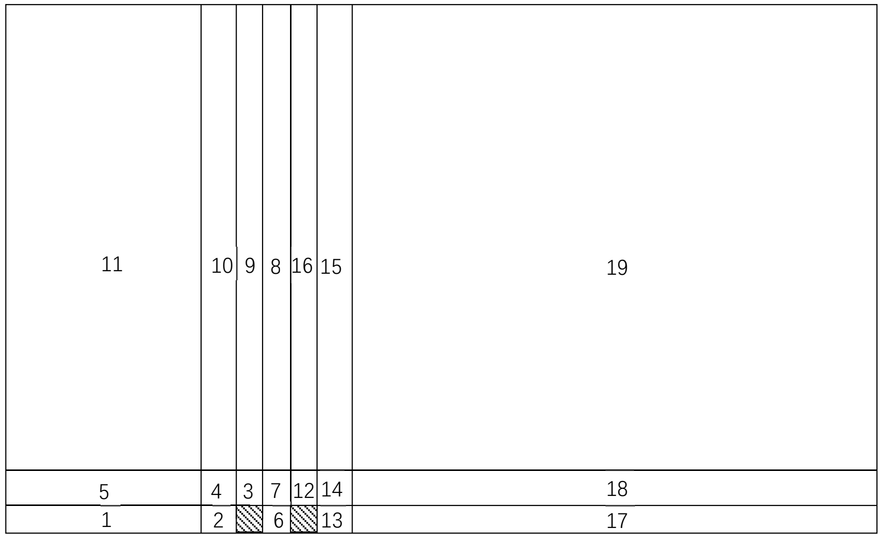

Figure 4.9: Block partition for the two cylinders simulation

be measured to tell users about the mesh quality: skewness measures the distance between the intersection of the lines connecting two cell centres with their common face, Usually a small skewness leads to the best results; mesh non-orthogonality measures the angle between the line connecting two cell centres and the normal line of their common face, 0 is the best value; aspect ratio (2D mesh) measures the ratio of the long edge to the short edge for all elements, 1.0 is the best value. Based on these factors, a mesh for the simulation of one cylinder is created and its global view is in Figure 4.10. In this mesh, all elements have perfect zero skewness and zero orthogonality due to the simple geometries of domain and cylinder. Optimal square shaped elements (aspect ratio equals to one) are assigned around the cylinder (see Figure 4.11), which ensures the finest solution in this area. Away from the cylinder, the grids are stretched and accordingly their aspect ratios grow. The highest aspect ratio occurs at the right downside corner of the domain, around 95 for the most stretched mesh. It is large but still smaller than 100, which is the upper limit of recommended aspect ratio in OpenFOAM . The same mesh configurations are also applied to the simulation of two cylinders, as in Figure 4.12.

The present study focuses on flows characterized by a low Reynolds number, so the wall function is not used. The velocity profile inside the viscous sublayer is directly modelled by grids. This requires that at least one cell should be inside the viscous sublayer, so that the viscous sublayer can be captured. Thus, the first node close to the bed and to the cylinder needs to have the value of $y^+ < 3$ to 5. In the present cases, the maximum value of y^+ is around 2.0 for the

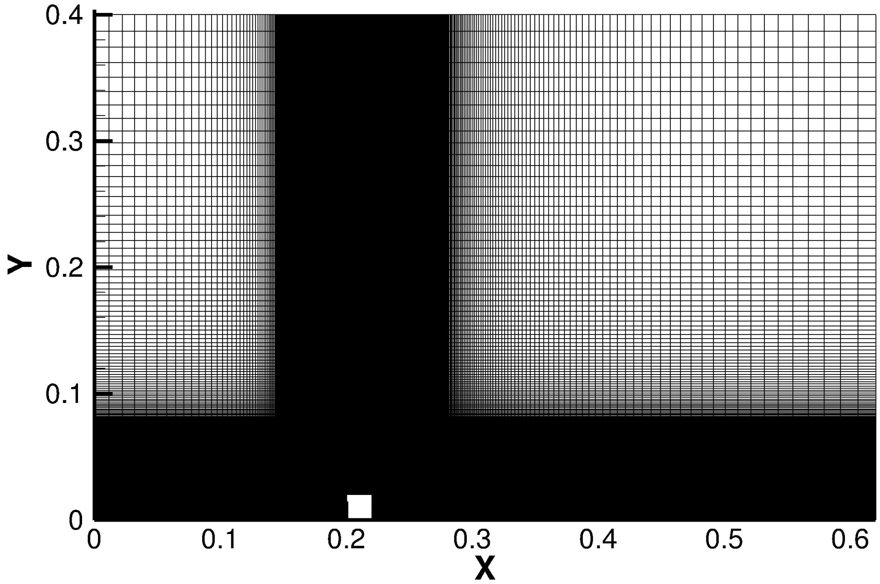

Figure 4.10: Global view of 80 × 80 mesh for the one cylinder simulation

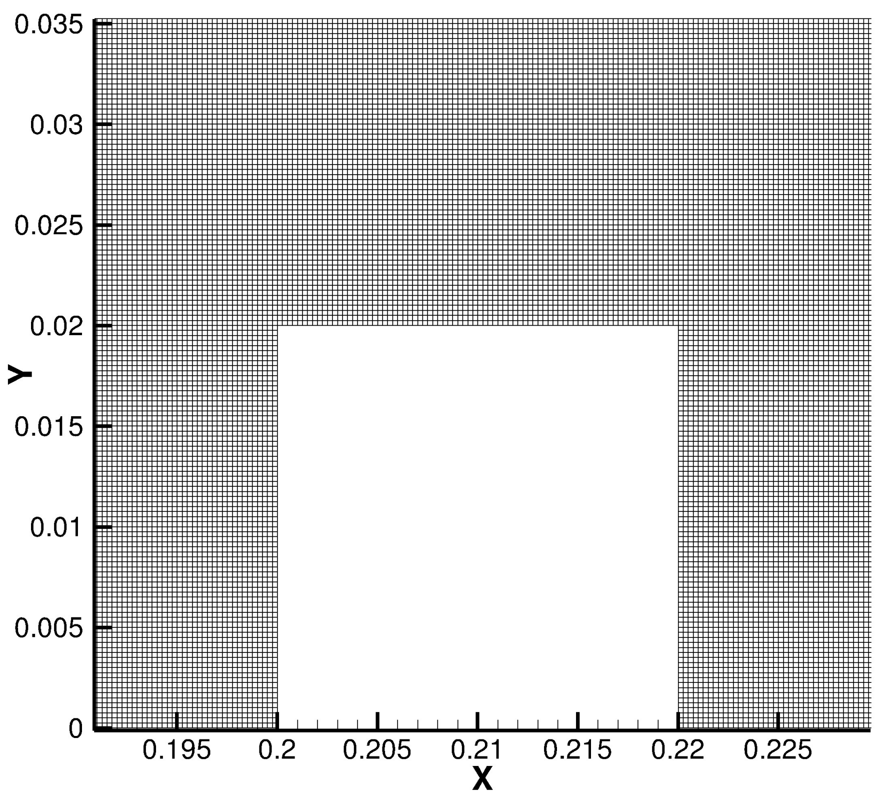

Figure 4.11: Local view of the 80 × 80 mesh for the one cylinder simulation

coarsest 40×40 mesh. Better values of the maximum y^+ are expected for finer 80×80 mesh and 160×160 mesh, which are small enough to model the viscous sublayer.

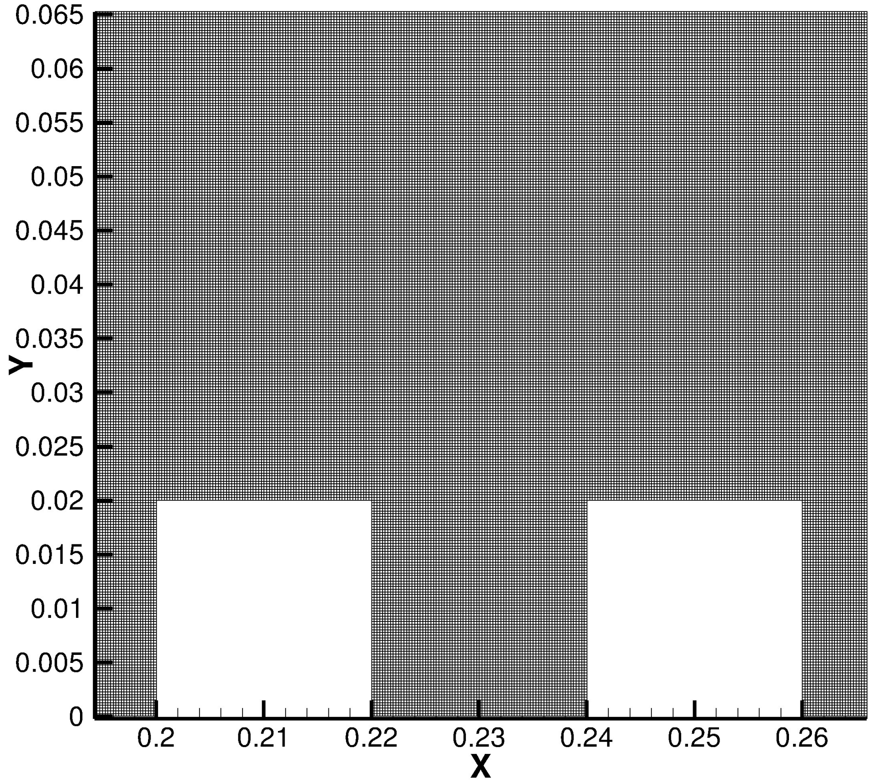

Figure 4.12: Local view of the 160×160 mesh for the two cylinders simulation

4.3 Boundary conditions

Boundary conditions are important in modelling the physics correctly. Boundary conditions can consist in fixed values on the boundaries or in gradients of the dependent variables. In the present RANS $k-\omega$ model, the equations include RANS equations and the conservation equations for k and ω, thus boundary conditions for U, V, k and ω at inlet, outlet, sea bed, top surface and the cylinder surface need to be specified. Additionally, initial values for the internal field need also to be specified.

An uniform constant horizontal velocity $U = U_0$ is given on the inlet, and the vertical velocity V is set to be zero. Dirichlet boundary conditions (Non-slip boundary conditions) $U = 0, V = 0$ are specified on the surface of the cylinder and the sea bed, Neumann boundary conditions are applied on the top surface and the outlet, where the values of velocity gradients are set to zero.

Pressure should be continuous among the whole domain and only pressure difference is important. This implies Newman boundary conditions with zero gradient of pressure along all boundaries. However, in OpenFOAM, a reference value of pressure need to be specified. So we assign a Dirichlet boundary condition with fixed pressure $p = 0$ at the outlet.

The mean turbulent kinetic energy k is defined in Equation 2.35. When it is close to the solid wall, the turbulent velocities should decay to zero as well as the kinetic energy k. This implies a Dirichlet boundary condition of $k = 0$ on the cylinder surface and the sea bed. Except the boundary condition, a uniform initial internal field of k is also specified, the initial internal field value k_0 is calculated by

$$k_0 = \frac{1}{2}\left[(0.05U)^2 + (0.05V)^2\right] \tag{4.1}$$

here 5% of the inlet velocity is taken to be the initial turbulence.

According to Wilcox (1988), ω can be calculated by eddy viscosity ratio and mean turbulent kinetic energy

$$\omega = \frac{\rho k}{\mu}\left(\frac{\mu_t}{\mu}\right)^{-1} \tag{4.2}$$

where μ_t is turbulent dynamic viscosity.

An uniform initial interval field of ω_0 is calculated by substituting the initial value of k_0 into Equation 4.2). When it is approaching the solid surface, ω should also decay to zero value. So boundary value $\omega = 0$ is applied on the sea bed and the surface of cylinder.

Chapter 5

Results and discussions

This chapter presents the results of RANS simulations for a uniform flow (Re=4000) around single and two wall-mounted square cylinders. The geometries, numerical methods and boundary conditions have been defined in Chapter 2 and Chapter 3. Force coefficients, pressure field and velocity field are discussed.

5.1 Flow around single cylinder

5.1.1 Mesh convergence test

In order to ensure mesh independence of the simulations, mesh convergence test is necessary. The test chooses a series of meshes with an successively increasing resolution. The solutions of these meshes are compared to find the optimal one. An optimal mesh should have the least computational consumption and a sufficient accuracy. When a mesh is determined, the mesh is applied to all of the simulations.

In this study, a layout of mesh grids is denoted by the number of elements in horizontal multiplying the number of elements in vertical along the edges of the cylinder. We select a group of meshes 40×40, 80×80 and 160×160 to test the convergence. These meshes differ each other mainly on the number of grids inside the blocks 2, 3, 4, 6 and 7 in Figure 4.8. Mesh grids inside other blocks are consistent.

The results of drag coefficient C_D and lift coefficient C_L are discussed to test the convergence.

In OpenFOAM, the drag and lift coefficients are exported in the form of time history, but the present study is steady-state. Thus, iteration number is used instead of time history. A typical example of iterations is shown in Figure 5.1. In this steady-state part of iterations, one of the most noteworthy characteristic is that although the drag and lift coefficients fluctuate, but their mean values over the whole iterations maintain unchanged. Therefore, the mean values of drag and lift coefficients over a enough large number of iterations (2000 to 5000) in the steady-state are determined to represent the solution of mesh.

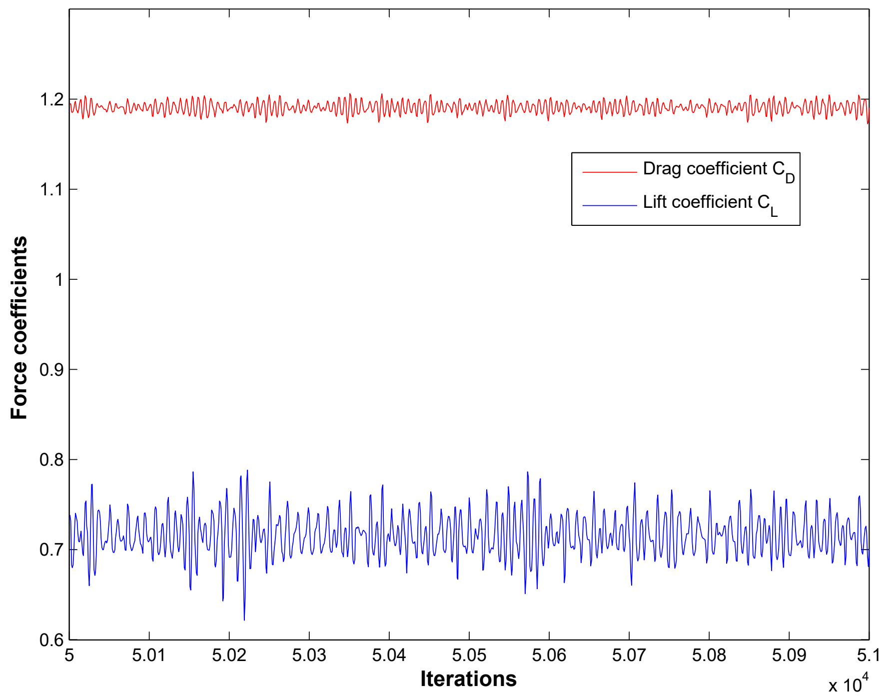

Figure 5.1: Fluctuation of force coefficients with respect to iteration number (80 × 80 mesh)

The solutions for the three meshes (40 × 40, 80 × 80 and 160 × 160) are shown in Table 5.1 and Figure 5.2. Figure 5.2 shows that the hydrodynamic quantities converge with the increase of mesh resolution. It is observe that the results of lift coefficient are consistent for the mesh 40 × 40 and 80 × 80, while the difference in drag coefficient between them reaches 3%. This implies that

Table 5.1: Hydrodynamic quantities for the mesh convergence test

Mesh	Drag coefficient C_D	Lift coefficient C_L	element numbers
40 × 40	1.09	0.716	72500
80 × 80	1.19	0.716	201500
160 × 160	1.21	0.733	349600

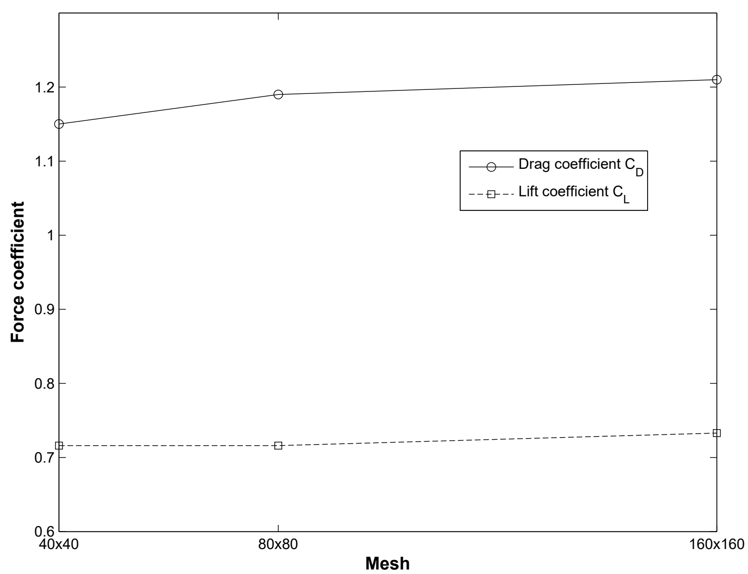

Figure 5.2: Variation of drag coefficient C_D and lift coefficient C_L to the meshes 40×40, 80×80 and 160×160

although the mesh 40×40 is fine enough to capture eddies on the top face of the cylinder, there are phenomena happening in a smaller scales in the front and backward cylinder faces that lie outside the 40×40 mesh's capability of detection. If we further increase the mesh resolution to the mesh 160×160, the difference in drag coefficient drops to 1.68% compared to the results of 80×80. Such small value demonstrates the mesh independence of drag coefficient. However, the values of lift coefficient have an unusual rise. One possible explanation is the fluctuation of convergence test: because the numerical approximation to exact convergent solution with increasing mesh quality is not perfect, the solution of fine mesh may fluctuate around the exact value (analytical solution). Moreover, the difference in lift coefficient is smaller than 2%, which still validate the mesh independence.

Above all, the 80×80 mesh is fine enough to capture necessary flow details in the one cylinder simulation. Thus, the discussion in the following sections is based on the solution of this mesh.

5.1.2 Pressure field

Pressure is an important parameter and is the source of drag and lift forces. In Figure 5.3, a contour plot of pressure is presented, which provides a direct view of pressure distribution across the domain. In the Figure, most of the domain is green (zero value), because the reference zero pressure is set on the outlet. Those areas that unaffected by the cylinder have zero local pressure. This also demonstrates the domain independence of the simulation that the cylinder-affected flow field is limited inside the domain. Besides, There is a large low pressure zone in the right side of the cylinder, which can be related to the effect of a large recirculation/vortex. This can be demonstrated if we compare the pressure contour in Figure 5.3 with streamlines in Figure 5.9), the vortex and low pressure area is corresponding well.

In order to have a closer view of pressure distribution, a local pressure contour is given in Figure 5.4. We find that the pressure is negative at the top of the cylinder. Because when flow hits the cylinder, it is stuck and deflected by the front face. To preserve the mass conservation, the flow has to pass the top face with a higher velocity. From the well-known Bernoulli equation, a high flow velocity results in a dropped local pressure. This explains the low pressure zone at the top face, and why the lift coefficient is negative. Moreover, the high pressure zone in front of the cylinder results also from the blocking effect of the cylinder. In the comparison of two zones,

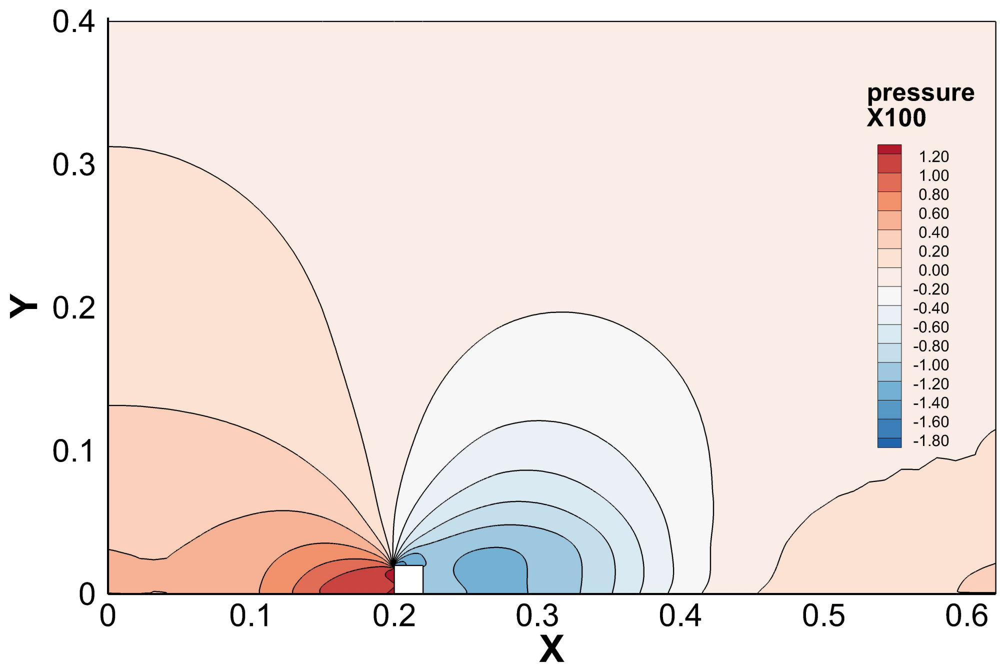

Figure 5.3: Pressure contour for the one cylinder simulation

it is noticed that this big difference in pressure creates drag force.

The effect of pressure on the cylinder is more obvious if we plot the distribution of pressure coefficient C_p. C_p is an parameter that represents the non-dimensional pressure, it is defined as Pressure coeffcient C_p is defined by

$$C_p = \frac{P}{0.5\rho\hat{U}^2} \tag{5.1}$$

The distribution of pressure coefficient C_p along the edges of the cylinder is shown in Figure 5.5. The lowest pressure coefficient -0.0008 is found at the point of the up-left corner B, which indicates the highest speed flow across here. The highest pressure coefficient is around 0.0007 between point A and point B, which implies that the front face $A-B$ forces the flow to turn around vertically. Thus, a high normal pressure is created at here. After that, pressure increases slowly along the edge of $B-C$. This is due to the reduction of velocity when flow spreads out after passing point B. Along the last edge of $C-D$, the pressure coefficient grows a little but does not recover to zero pressure, due to the large vortex with low pressure behind the cylinder.

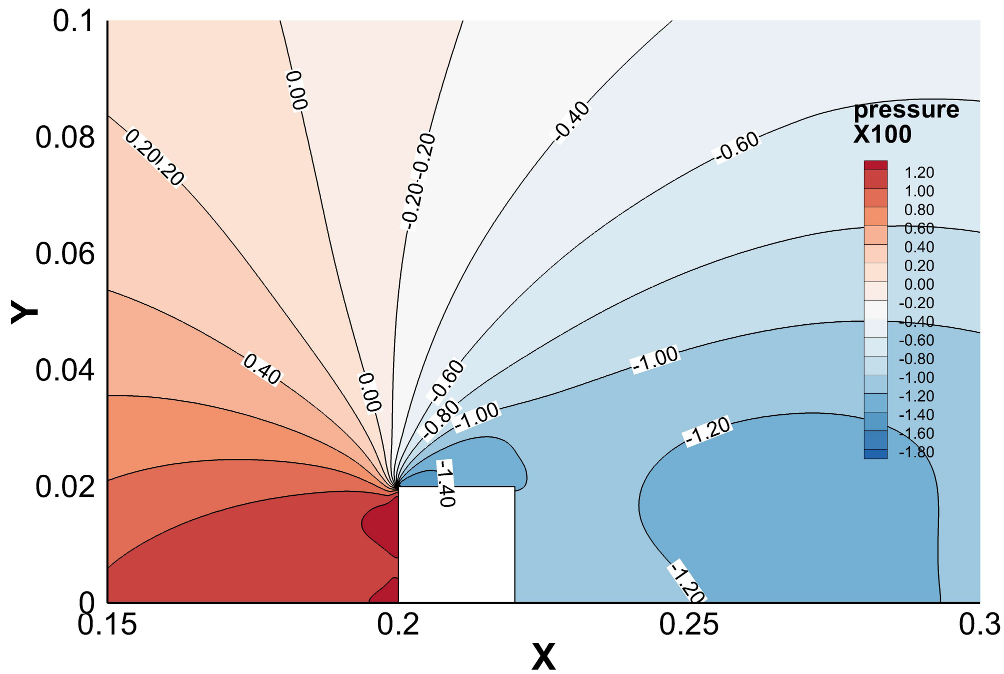

Figure 5.4: Local view of pressure distribution around the cylinder

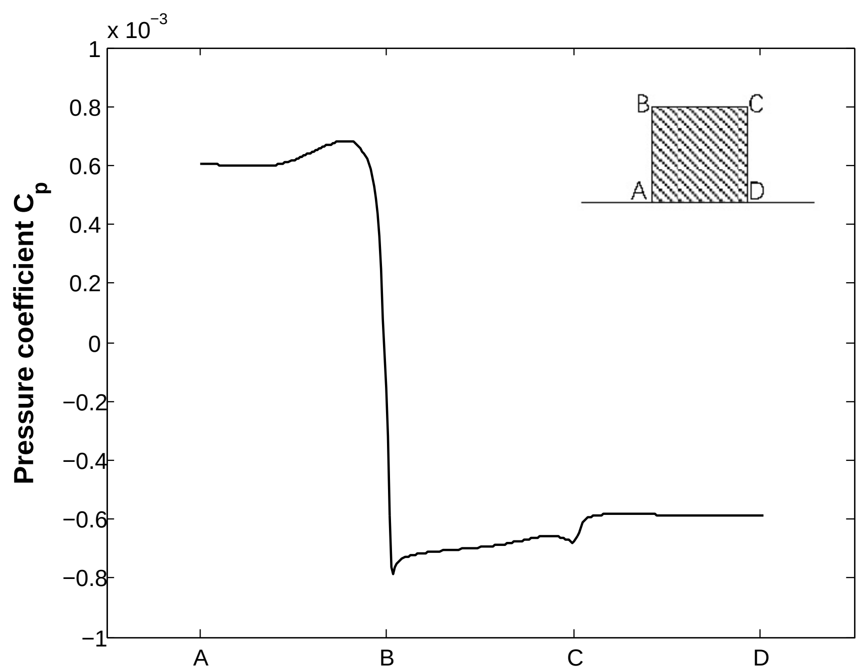

Figure 5.5: Pressure coefficient along the edges of the cylinder

5.1.3 Velocity field

Contour plot of horizontal velocity component is given in Figure 5.6. One can observe that the blocking effect of the cylinder creates a small sluggish area (yellow) in front of it. Accordingly, there is a velocity surplus area spread out from the point B. However, an unexpected low area is shown at the left side of the cylinder that can not be identified from the pressure contour, which indicates a vortex in this position.

The negative velocity zone behind the cylinder corresponds to a large vortex that is visible in Figure 5.3 with negative pressure. This large vortex forces the flow to turn around, producing a splash of high velocity zone above it.

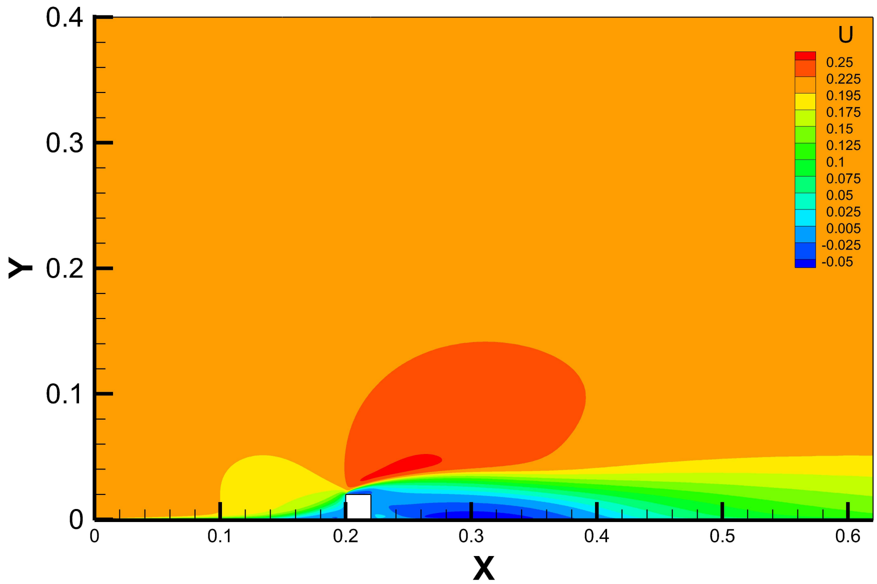

Figure 5.6: Velocity contour for the one cylinder simulation

The plot of streamlines is presented in Figure 5.7. There are total three large vortices shown in the figure, which have excellent agreements with the pressure and velocity contours. The two vortices attached to the left and the right cylinder faces are clockwise and anticlockwise respectively, while the largest vortex behind the cylinder is clockwise. However, if we get a closer view to the cylinder, there are two inconspicuous vortices at the two downward corners of the cylinder that are invisible in Figure 5.7. These two small vortices are induced by the two larger vortices above them. The positions and strength of the vortices are consistent with the published work, e.g. in Figure 1.1. Thus, it validates that the present RANS simulation is credible in

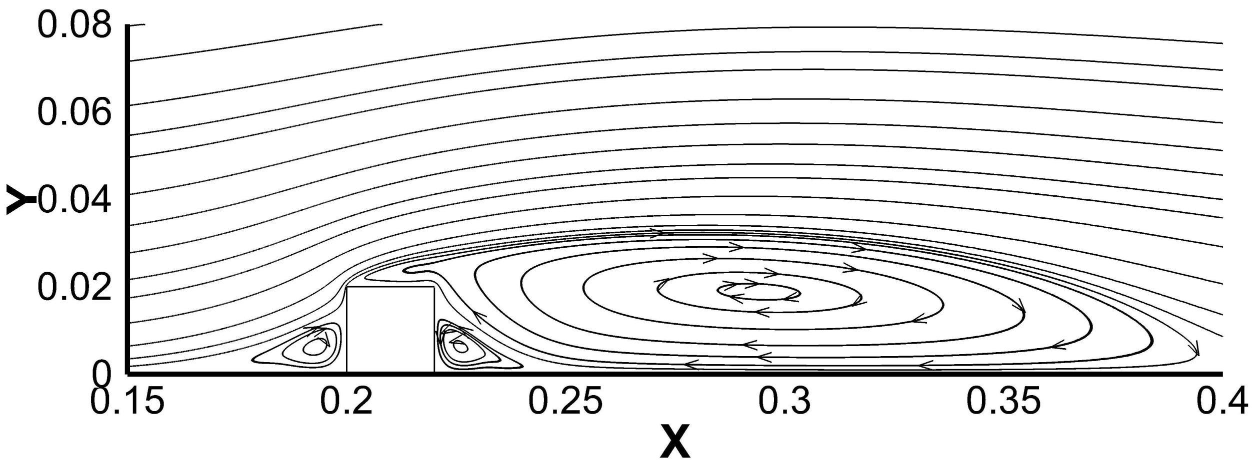

Figure 5.7: Streamlines for the one cylinder simulation

predicting flow behaviors for flow around cylinder.

5.2 Flow around two square cylinder

This section presents the results of RANS simulation for a uniform flow (Re=4000) around two wall-mounted square cylinders with three intervals. The three intervals are set be $L = h$, $L = 2h$ and $L = 5h$. Accordingly, we name them case 1, case 2 and case 3.

Flow around two square cylinders generates many flow behaviors such as small scale of vortices, flow circulations and collisions. These flow behaviors exist especially inside the interval, which differs it from the one square cylinder case. It is expected that as the distance between the two square cylinders increases, the second cylinder moves gradually away from the influence of the eddies generated by the first cylinder. The discussion to the pressure distribution and velocity field during this process is illustrated.

5.2.1 Mesh convergence tests

Mesh convergence tests are performed for the three cases separately. Because of the complex interactions between the two square cylinders, It is expected that much smaller scales of flow phenomena should happen between the two cylinders compared to the one cylinder case. Thus, more details need to be captured with a finer grid. In the convergence tests, results for a set of higher mesh resolutions: mesh 80×80, mesh 120×120 and mesh 160×160 are presented. Force coefficients on each cylinder are calculated and compared to each other to validate the mesh convergence.

Table 5.2: Covergence tests for the simulation of two square cylinders. C_{D1}: drag coefficient of the first cylinder; C_{L1}: lift coefficient of the first cylinder; C_{D2}: drag coefficient of the second cylinder; C_{L2}: lift coefficient of the second cylinder.

Test case 1: $L = h$

mesh	drag coefficient C_{D1}	lift coefficient C_{L1}	drag coefficient C_{D2}	lift coefficient C_{L2}
80×80	1.457	1.083	-0.550	0.545
120×120	1.491	1.126	-0.589	0.533
160×160	1.505	1.145	-0.597	0.515

Test case 1: $L = 2h$

mesh	drag coefficient C_{D1}	lift coefficient C_{L1}	drag coefficient C_{D2}	lift coefficient C_{L2}
80×80	1.472	1.029	-0.659	0.309
120×120	1.487	1.032	-0.657	0.305
160×160	1.492	1.032	-0.658	0.299

Test case 3: $L = 5h$

mesh	drag coefficient C_{D1}	lift coefficient C_{L1}	drag coefficient C_{D2}	lift coefficient C_{L2}
80×80	1.248	0.794	-0.291	0.164
120×120	1.260	0.796	-0.281	0.162
160×160	1.262	0.794	-0.280	0.158

Table 5.2 and Figure 5.8 shows the solutions of the convergence tests. Force coefficients are measured by averaging over an enough large number of iterations (2000 to 5000 iterations) after the simulations reach steady state. C_{D1} and C_{D2} represent drag coefficients on the first and second cylinder respectively, and C_{L1} and C_{L2} are lift coefficients of the first and second cylinder respectively.

Comparing the solutions of the mesh 80×80 and the mesh 120×120 , we can find that the maximum difference in drag coefficient is 7.1%, and the maximum 4% difference is found for lift coefficient. This proves our guess that smaller eddies are generated and they are missed by the 80×80 mesh grid.

If we further increase the mesh to 160×160, the force coefficients starts to show mesh independence. Comparing the results of three cases between the 120×120 mesh and the 160×160

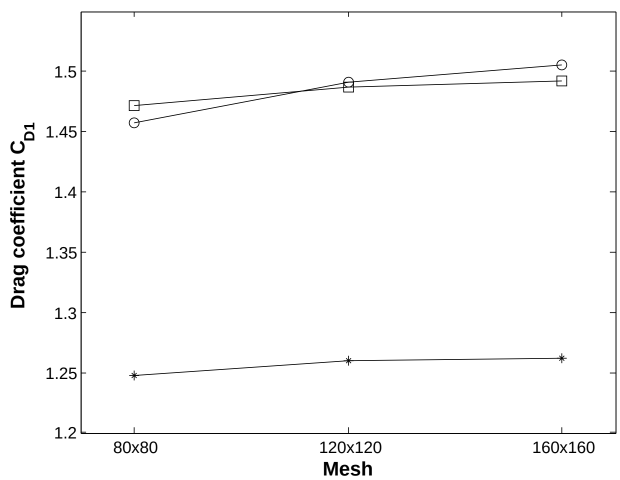

(a) Variation of drag coefficient C_{D1}

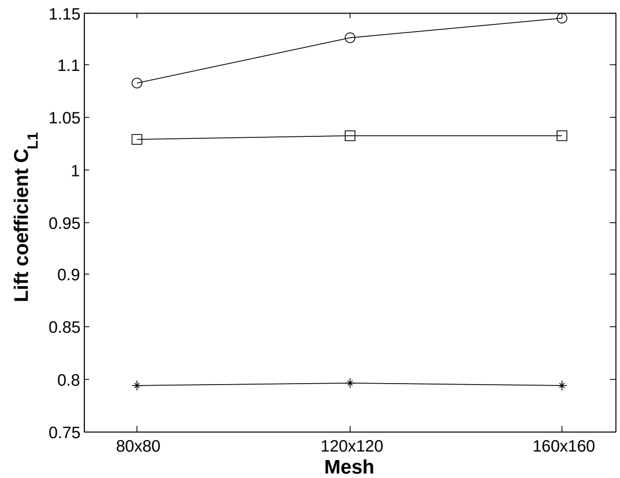

(b) Variation of lift coefficient C_{L1}

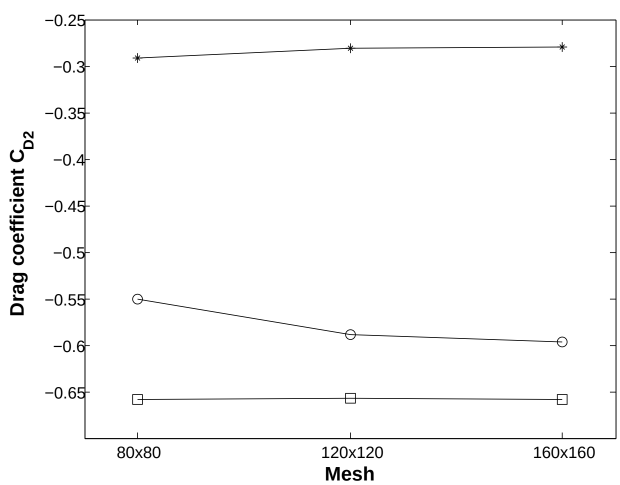

(c) Variation of drag coefficient C_{D2}

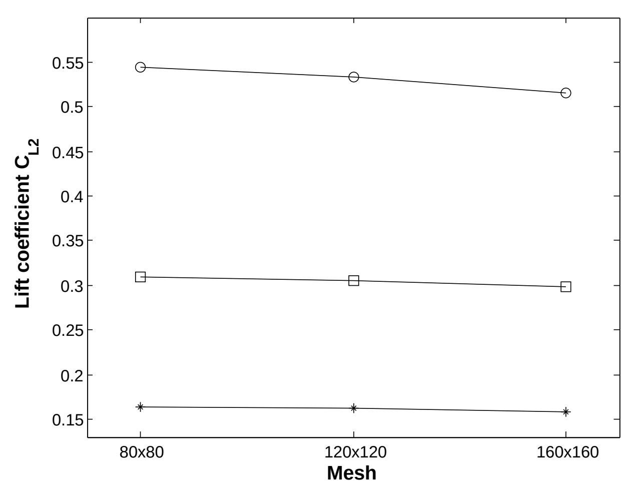

(d) Variation of lift coefficient C_{L2}

Figure 5.8: Variations of force coefficients to the the meshes 80×80, 120×120 and 160×160. C_{D1}: drag coefficient of the first cylinder; C_{L1}: lift coefficient of the first cylinder; C_{D2}: drag coefficient of the second cylinder; C_{L2}: lift coefficient of the second cylinder. $\circ$: results for the case $L = h$; $\square$: results for the case $L = 2h$; $*$: results for the case $L = 5h$.

mesh, we find the maximum relative difference of C_{D1} is less than 1%, and the maximum difference in C_{L1} is around 1.6%. The maximum difference of C_{D2} is also less than 1%. However, the difference of the lift coefficient C_{L2} for the case 1 is up to 3.3% (0.533 versus 0.515). Besides, it is noticed that the largest differences in force coefficients are always found at the second cylinder, especially in the case 1 with $L = h$. It can be explained that the complicated flow interactions between the two cylinders generate many tiny eddies and subsequently they are transported to the downstream second cylinder. Thus, the second cylinder is very sensitive to the flow phenomena inside the interval. These tiny eddies are particularly intensive in the case 1, where the strongest flow interaction happens in this case. Therefore, the mesh may not be able to capture the behaviors of all eddies, which results in the large difference in C_{L2}. For the larger interval of case 2 and case 3, the interactions become weaker, and the differences in C_{L2} are acceptable.

Although the 3.3% difference can not be considered ideally convergent, the solutions for other cases are satisfying. It can be sure that a denser mesh would give better result than 3.3% for C_{L2}. So the solutions of the 160×160 mesh are considered to be mesh independent. The 160×160 mesh is applied for the simulations of two square cylinders.

5.2.2 Pressure fields

Pressure isocontours for the three cases are shown in Figure 5.9.

In the first pressure isocontour for the test case 1 with $L = h$, several low pressure zones are visible between the two cylinders. The first low pressure zone is on top of the first cylinder. This zone is created by the high speed flow after it separates at the up-left bluff corner of the cylinder, which forms a vortex on the top face. Between the cylinders, two low pressure circular zones are arranged vertically. They are the results of two vortices in here. After the second cylinder, a huge half circular low pressure zone is shown, whose shape is similar to the pressure isocontour of the one cylinder simulation at the same place but with smaller size. Its magnitude (0.0063) is also only around half of the one cylinder simulation's one (0.012), which indicates the vortex in the one cylinder simulation is stronger.

In the second pressure isocontour for the test case 2 $L = 2h$, we find a significant difference to the case 1: a big vortex replaces the position of the two vertical arrayed ones and fills up the whole inner space formed by the two cylinders. It is also worth noting that the huge half circular

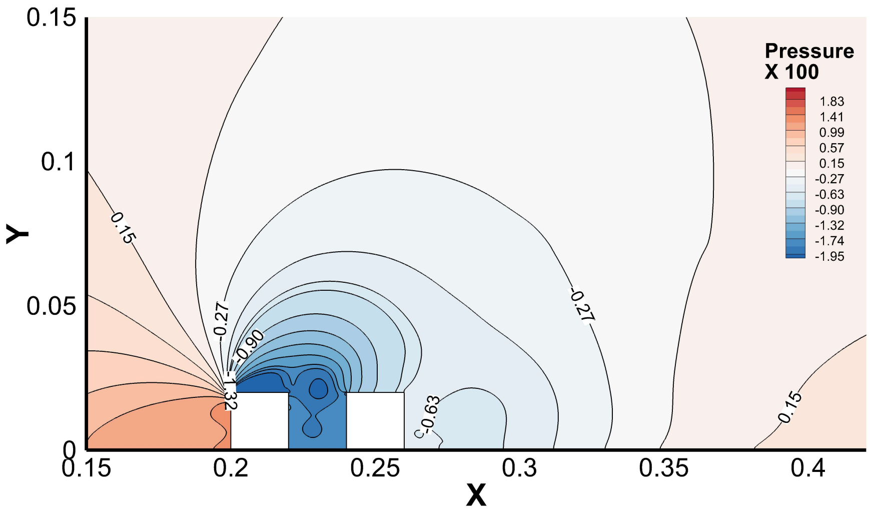

(a) Pressure isocontour for the case 1 with $L = h$

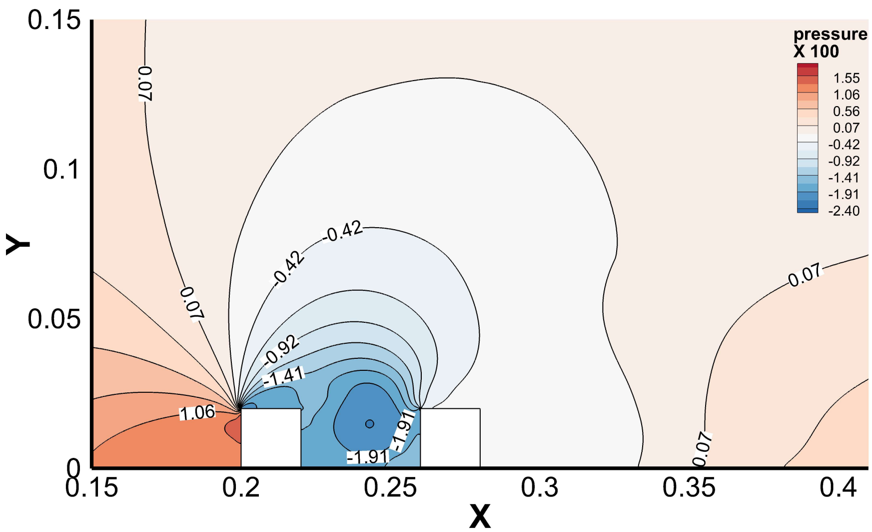

(b) Pressure isocontour for the case 2 with $L = 2h$

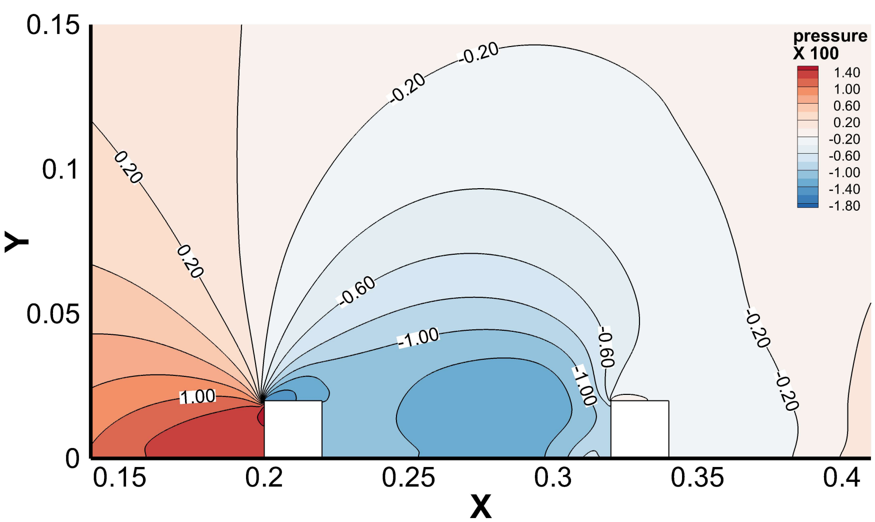

(c) Pressure isocontour for the case 3 with $L = 5h$

Figure 5.9: Pressure isocontours for the three test cases

low pressure zone disappears in this case. In fact, the vortex still exists but it becomes so weak that the present levels of pressure legend can not catch it.

For the last pressure isocontour of the case 3 with $L = 5h$, the only vortex in the case 2 between the two cylinders becomes larger. One explanation is that the larger interval provides space for the vortex to further develop and with smaller resistance from the second cylinder. It should be also noted that the pressure just behind the second cylinder becomes even smaller, which indicates a even weaker vortex.

Dimensionless integrals of pressure along the edges of the cylinder gives force coefficients. If we look at the force coefficients in Table 5.2 for the adopted mesh 160×160. The existence of the second cylinder improves the C_{D1} up to 25% and the C_{L1} up to 56% for the case 1 relative to force coefficients in Table 5.1. This implies taht the strongest interaction between the two cylinders happens in the case 1. While in the case 3, the C_{L1} has only 8% difference relative to the one cylinder simulation. The C_{D1} has even less than 4% difference. The influence of second cylinder in the case 3 can be ignored.

5.2.3 Velocity fields

Velocity contours of the horizontal velocity component U for the three test cases are presented in Figure 5.10. It is observed that the velocity distribution in front of the first cylinder is consistent for Figure 5.6) and Figure 5.10. However, the velocity surplus area (red) after the separation point in Figure 5.10 is much smaller than the one in Figure 5.6. By the observation, this can be explained that the existence of the second cylinder blocks the velocity field and stops its further growth. Inside the interval, The low velocity zones (blue) in the three cases correspond well with the low pressure areas in Figure 5.9, which indicates the same information of flow phenomenon in these areas.

Comparing the three figures, we also observe that the affected area in the downstream direction becomes larger with the increasing interval.

More information can be extracted from streamlines (see Figure 5.11). It can be found that the flow forms a clockwise vortex in front of the left face when it hits the first cylinder. The flow separates when it pass the up-left cylindrical corner. The separated flow experiences complex interactions with the second cylinder, resulting in different flow phenomena for the three cases.

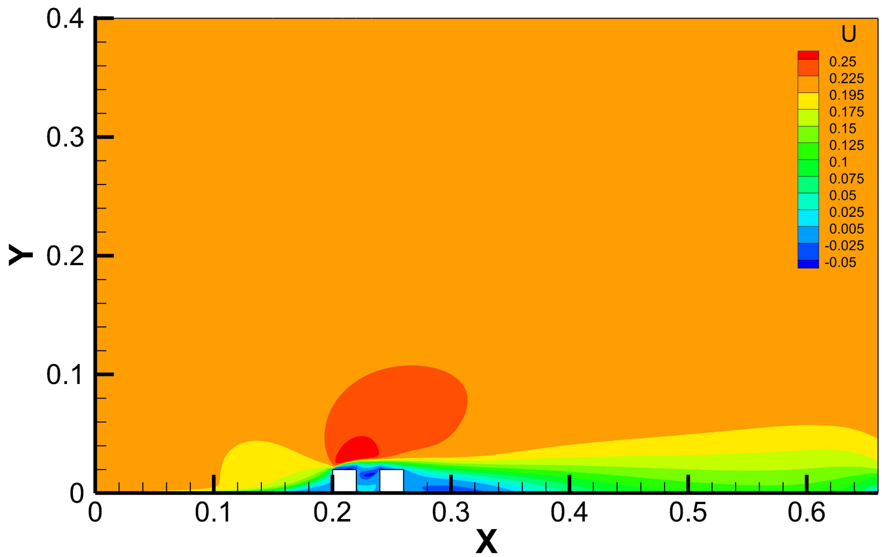

(a) Velocity contour for the case 1 with $L = h$

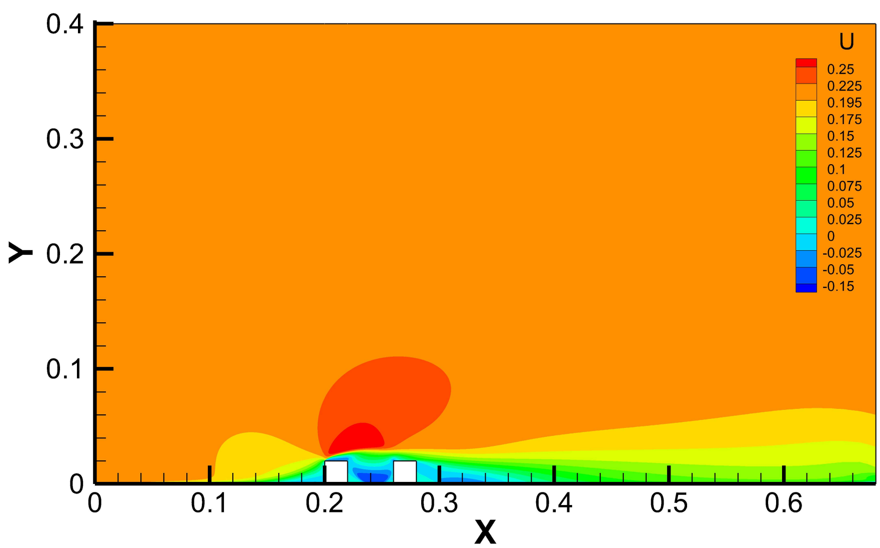

(b) Velocity contour for the case 2 with $L = 2h$

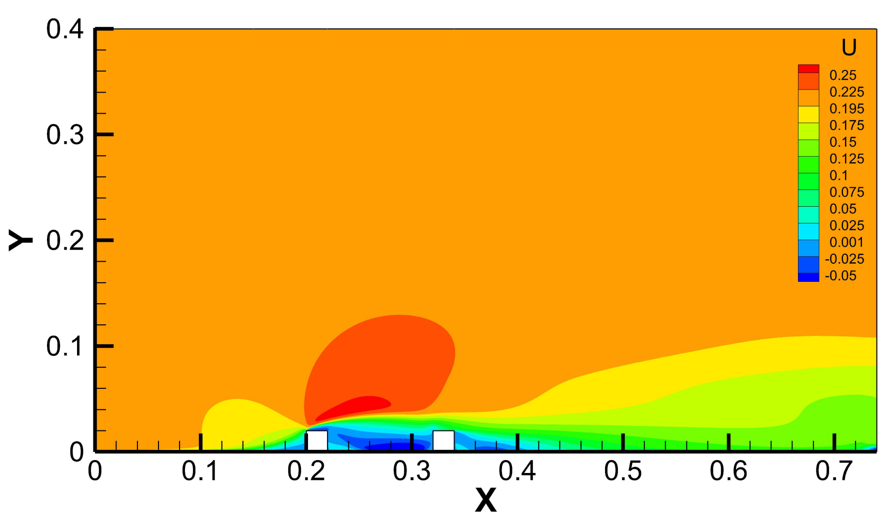

(c) Velocity contour for the case 3 with $L = 5h$

Figure 5.10: Velocity contours for the three cases

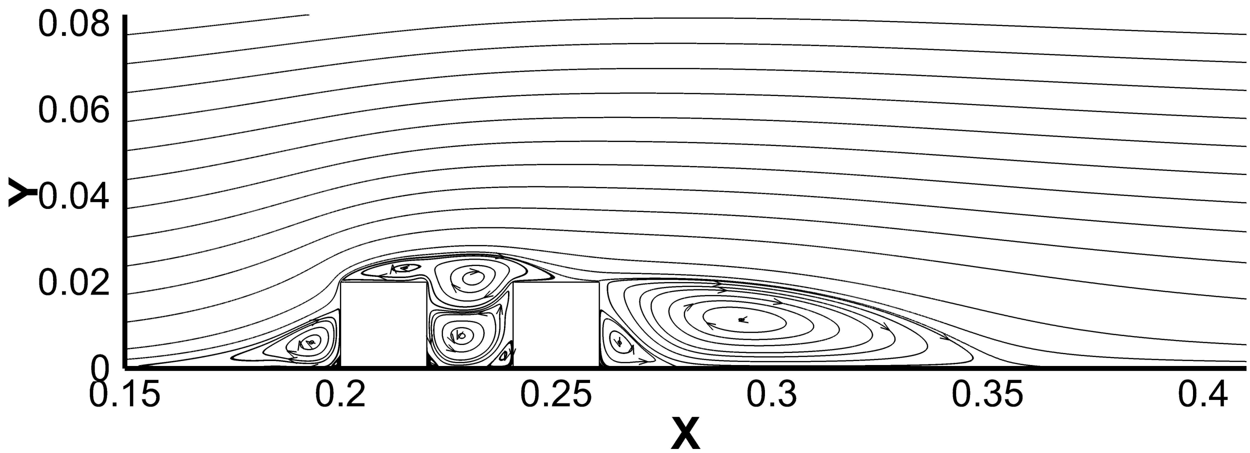

(a) Streamlines for the case 1 with $L = h$

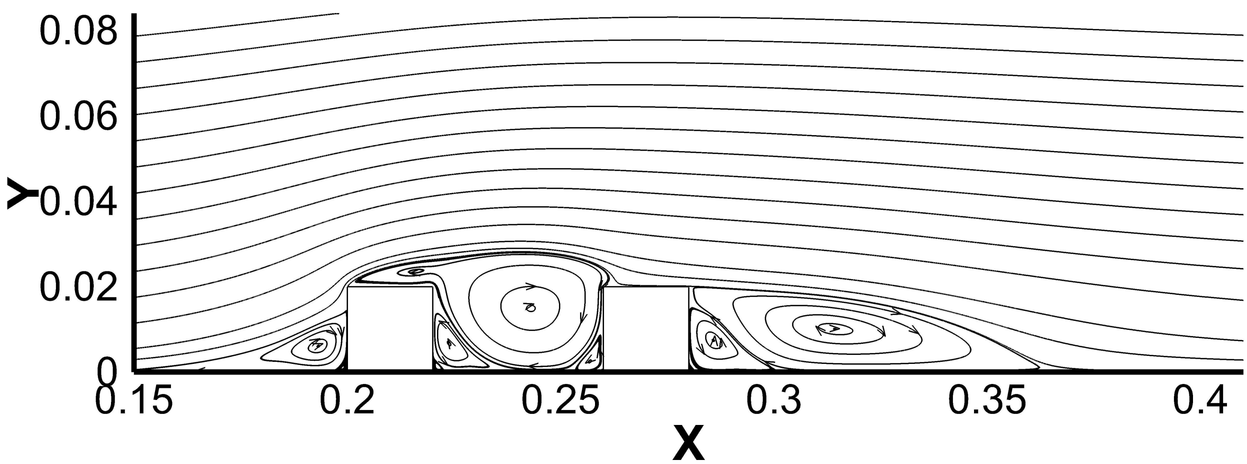

(b) Streamlines for the case 2 with $L = 2h$

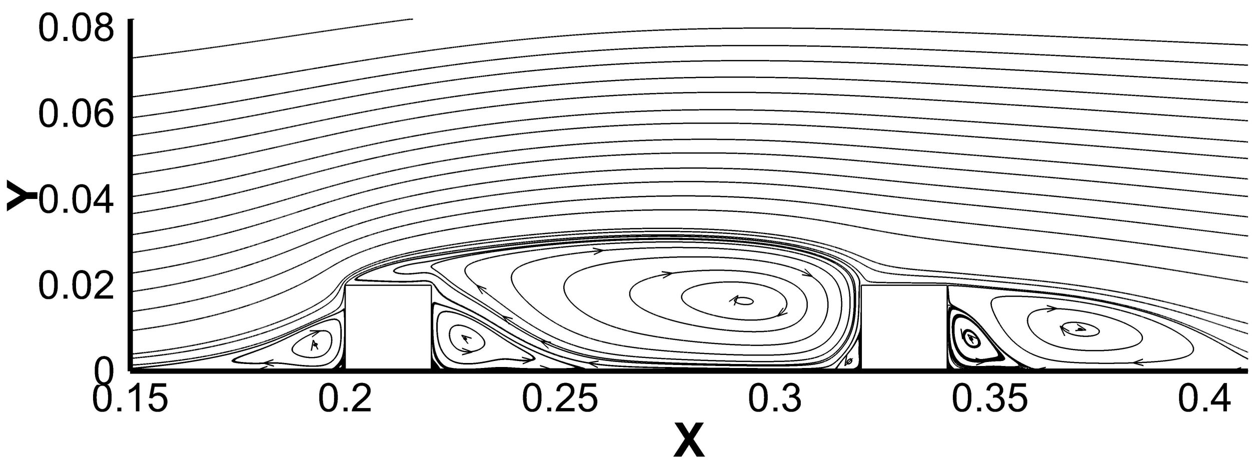

(c) Streamlines for the case 3 with $L = 5h$

Figure 5.11: Streamlines for the three cases

In the streamlines Figure 5.11(a), two vortices are shown together vertically at the middle square space, which corresponds to the two low pressure zones in Figure 5.9. The higher vortex is clockwise and is generated by the separated flow from the first cylinder. However, the interval is so narrow that the higher vortex is forced to reattach the top surface of the second cylinder, while it should have reattached the wall if the second cylinder does not exist, as shown in Figure 5.7. The reattachment "lift" the vortex and creates a closed space below it. The flow motion inside this closed space is similar to the lib-driven cavity flow problem. The recirculation flow at its top drives the fluid to form an another vortex, with direction opposite to the higher one. After the second cylinder, the flow behaviors are consistent with Figure 5.7. The two cylinders interact with the flow as a whole body.

When the interval is further increased to two length, it becomes large enough that there is only one big clockwise vortex inside this space (Figure 5.11(b)). Consequently, the reattachment on the second cylinder disappears. The same situation also happens for the case 3 in Figure 5.11(c). It is noteworthy that the small vortex on top of the first cylinder in Figure 5.11(a) and (b) disappears, which can be also attributed to the consequence of a larger interval.

The vortices illustrated above can be found and correspond well to the pressure and the velocity field in Figure 5.10 and Figure 5.9. However, there are some vortices in the streamlines that can not be simply recognized from the velocity and the pressure contours. For example, there are four vortices attached to the left and right faces of the two cylinders respectively in Figure 5.11, and they can not be all clearly identified from the velocity and pressure contours. The two vortices attached to the first cylinder are clockwise for the left one and anticlockwise for the right one, while the other two vortices are in the opposite directions that the left one is anticlockwise and the right one is clockwise. Moreover, there are another four tiny vortices below the four big ones at each downside right angle corner, which cannot even be seen from the streamlines. Their rotations are reverse to the vortices above them.

Above all, we can conclude that with the increase of distance between the two cylinders, the two cylinders suffer less impacts from each other.

Chapter 6

Conclusion and recommendations for future work

Numerical simulations of a uniform flow (Re=4000) around single and two 2D square cylinders on the sea bed have been performed. A low-Re RANS equations with standard $k-\omega$ turbulence model have been applied.

To minimize any uncertainties related to mesh quality, mesh convergence tests are conducted for the simulations. Iteration-averaged values of drag coefficient C_D and lift coefficient C_L in steady-state for a set of meshes are compared. The tests have proved that the adopted meshes are appropriate and the solutions are convergent.

In the simulation of flow around one square cylinder, the resulting streamlines are in agreement with published simulations. Streamlines, velocity contours and pressure contours corresponds well with each other at the positions of vortex and flow reattachment. This indicates that the RANS equations with $k-\omega$ turbulence model predicts flow behaviors accurately.

Results from the numerical simulations of flow around two square cylinders for three different intervals (($L = h, 2h$ and $5h$, with names case 1, 2 and 3) have been discussed. The strongest interactions between the two cylinders are found in the case 1. The two cylinders interact with the flow as a whole body. With the increasing interval, the interactions become weaker. The two cylinders suffer less impact from each other. A very unique lib-driven cavity flow is only shown in the case 1 and disappears for larger interval. Besides, the small vortex on top of the first cylinder disappears in the case 3, and the reattachment of vortex (generated by the first cylinder) to the second cylinder also disappears in the case 2 and the case 3, which indicates less influence from the second cylinder. The big recirculation zone behind the second cylinder is smaller and weaker with the increasing interval. For the largest interval $L = 5h$, drag coefficient of the first cylinder has only 4% difference relative to the one cylinder simulation. This indicates the interaction between the two cylinder is very weak, The two cylinders are independent.

However, the present works are insufficient. Some future works are recommended below:

1. The convergence test in the two cylinder simulation is not perfect. A denser group of meshes need to be tested to validate the convergence.

2. The present numerical simulations is two dimensional, but results from three dimensional simulation is closer to the real physical conditions. It would be of interest to study the hydrodynamic phenomenon of a full 3D analysis of cube and compare them with the present simulations.

3. By replacing RANS model by LES and DNS approach, more details of flow can be captured and some instinctive shortages of RANS can be overcomed. Three dimensional simulation would require transient simulation instead of steady-state, accordingly, the computational cost would be largely increased.

Bibliography

Baetke, F., Werner, H., and Wengle, H. (1990). Numerical simulation of turbulent flow over surface-mounted obstacles with sharp edges and corners. *Journal of Wind Engineering and Industrial Aerodynamics*, 35:129–147.

Bearman, P. and Zdravkovich, M. (1978). Flow around a circular cylinder near a plane boundary. *Journal of Fluid Mechanics*, 89(01):33–47.

Boussinesq, J. (1877). Théorie de l'écoulement tourbillant (theories of swirling flow), mém. prés. par div. savants à l'acad. *Sci. Paris*, 23.

Castro, I. and Robins, A. (1977). The flow around a surface-mounted cube in uniform and turbulent streams. *Journal of Fluid Mechanics*, 79(02):307–335.

Cheng, W.-C. and Porté-Agel, F. (2013). Evaluation of subgrid-scale models in large-eddy simulation of flow past a two-dimensional block. *International Journal of Heat and Fluid Flow*, 44:301–311.

Faltinsen, O. (1993). *Sea loads on ships and offshore structures*, volume 1. Cambridge university press.

Ferziger, J. H. and Peric, M. (2012). *Computational methods for fluid dynamics*. Springer Science & Business Media.

Greenshields, C. (2015). About OpenFOAM. http://cfd.direct/openfoam/about/.

Homann, F. (1936). Influence great toughness at flow around cylindrical. *Research in the field of engineering A*, 7(1):1–10.

Hoxey, R., Richards, P., and Short, J. (2002). A 6 m cube in an atmospheric boundary layer flow-part 1. full-scale and wind-tunnel results. *Wind and Structures*, 5(2_3_4):165–176.

Iaccarino, G., Ooi, A., Durbin, P., and Behnia, M. (2003). Reynolds averaged simulation of unsteady separated flow. *International Journal of Heat and Fluid Flow*, 24(2):147–156.

Kim, J., Moin, P., and Moser, R. (1987). Turbulence statistics in fully developed channel flow at low reynolds number. *Journal of fluid mechanics*, 177:133–166.

Kolmogorov, A. (1942). Equations of motion of an incompressible turbulent fluid. *Izv Akad Nauk SSSR Ser Phys*, 6:56–58.

Lakehal, D. and Rodi, W. (1997). Calculation of the flow past a surface-mounted cube with two-layer turbulence models. *Journal of Wind Engineering and Industrial Aerodynamics*, 67:65–78.

Landahl, M. T. and Mollo-Christensen, E. (1992). *Turbulence and random processes in fluid mechanics*. Cambridge University Press.

Lim, H. C., Thomas, T., and Castro, I. P. (2009). Flow around a cube in a turbulent boundary layer: LES and experiment. *Journal of Wind Engineering and Industrial Aerodynamics*, 97(2):96–109.

Moss, W. and Baker, S. (1980). Re-circulating flows associated with two-dimensional steps. *Aeronautical Quarterly*, 31:151–172.

Moukalled, F., Mangani, L., and Darwish, M. (2016). *The Finite Volume Method in Computational Fluid Dynamics*. Springer.

Murakami, S. and Mochida, A. (1995). On turbulent vortex shedding flow past 2D square cylinder predicted by CFD. *Journal of Wind Engineering and Industrial Aerodynamics*, 54:191–211.

Patankar, S. (1980). *Numerical heat transfer and fluid flow*. CRC press.

Peralta, C., Nugusse, H., Kokilavani, S., Schmidt, J., and Stoevesandt, B. (2014). Validation of the simpleFoam (RANS) solver for the atmospheric boundary layer in complex terrain. In *ITM Web of Conferences*, volume 2, page 01002. EDP Sciences.

Pope, S. B. (2001). Turbulent flows.

Pozrikidis, C. (2009). *Fluid dynamics: theory, computation, and numerical simulation.* Springer Science & Business Media.

Prandtl, L. (1925). Bericht über untersuchungen zur ausgebildeten turbulenz. *Z. Angew. Math. Mech*, 5(2):136–139.

Prandtl, L. and Wieghardt, K. (1947). *Über ein neues Formelsystem für die ausgebildete Turbulenz.* Vandenhoeck & Ruprecht.

Prsic, M. A. (2016). Numerical simulations of the flow around single and tandem circular cylinders close to a plane wall.

Roy, C. J., DeChant, L. J., Payne, J. L., and Blottner, F. G. (2003). Bluff-body flow simulations using hybrid RANS/LES. *AIAA Paper*, 3889:2003.

Schlichting, H. (1968). Boundary-layer theory.

Smagorinsky, J. (1963). General circulation experiments with the primitive equations: I. the basic experiment*. *Monthly weather review*, 91(3):99–164.

Sousa, J. (2002). Turbulent flow around a surface-mounted obstacle using 2D-3C DPIV. *Experiments in Fluids*, 33(6):854–862.

Stoesser, T., Mathey, F., Frohlich, J., and Rodi, W. (2003). LES of flow over multiple cubes. *Ercoftac Bulletin*, 56:15–19.

Tennekes, H. and Lumley, J. L. (1972). *A first course in turbulence.* MIT press.

Tian, X., Ong, M. C., Yang, J., and Myrhaug, D. (2013). Unsteady RANS simulations of flow around rectangular cylinders with different aspect ratios. *Ocean Engineering*, 58:208–216.

Wilcox, D. C. (1988). Reassessment of the scale-determining equation for advanced turbulence models. *AIAA journal*, 26(11):1299–1310.

Yakhot, A., Liu, H., and Nikitin, N. (2006). Turbulent flow around a wall-mounted cube: A direct numerical simulation. *International journal of heat and fluid flow*, 27(6):994–1009.